Boosting light-driven CO2 reduction into solar fuels: Mainstream avenues for engineering ZnO-based photocatalysts

Shilpa Patial, Rohit Kumar, Pankaj Raizada, Pardeep Singh, Quyet van Le, Eric Lichtfouse, Dang Le Tri Nguyen, Van-Huy Nguyen

▶ **To cite this version:**

Shilpa Patial, Rohit Kumar, Pankaj Raizada, Pardeep Singh, Quyet van Le, et al.. Boosting light-driven CO2 reduction into solar fuels: Mainstream avenues for engineering ZnO-based photocatalysts. Environmental Research, 2021, 197, pp.111134. 10.1016/j.envres.2021.111134 . hal-03255818

HAL Id: hal-03255818
https://hal.science/hal-03255818

Submitted on 9 Jun 2021

HAL is a multi-disciplinary open access archive for the deposit and dissemination of scientific research documents, whether they are published or not. The documents may come from teaching and research institutions in France or abroad, or from public or private research centers.

L'archive ouverte pluridisciplinaire **HAL**, est destinée au dépôt et à la diffusion de documents scientifiques de niveau recherche, publiés ou non, émanant des établissements d'enseignement et de recherche français ou étrangers, des laboratoires publics ou privés.

Environmental Research 197 (2021) 111134
https://doi.org/10.1016/j.envres.2021.111134

Boosting light-driven CO_2 reduction into solar fuels: Mainstream avenues for engineering ZnO-based photocatalysts

Shilpa Patial [a], Rohit Kumar [a], Pankaj Raizada [a,*], Pardeep Singh [a], Quyet Van Le [b], Eric Lichtfouse [c,d], Dang Le Tri Nguyen [e,f], Van-Huy Nguyen [g,**]

[a] School of Advanced Chemical Sciences, Faculty of Basic Sciences, Shoolini University, Solan (HP), 173229, India
[b] Institute of Research and Development, Duy Tan University, Da Nang, 550000, Vietnam
[c] Aix-Marseille Univ, CNRS, IRD, INRA, Coll France, CEREGE, Aix-en-Provence, 13100, France
[d] International Research Centre for Renewable Energy, State Key Laboratory of Multiphase Flow in Power Engineering, Xi'an Jiaotong University, Xi'an, PR China
[e] Division of Computational Physics, Institute for Computational Science, Ton Duc Thang University, Ho Chi Minh City, Vietnam
[f] Faculty of Applied Sciences, Ton Duc Thang University, Ho Chi Minh City, Vietnam
[g] Faculty of Biotechnology, Binh Duong University, Thu Dau Mot, Vietnam

ARTICLE INFO

Keywords:
Photocatalytic CO_2 reduction
Zinc oxide (ZnO)
Doping
Oxygen vacancies
Hetero-structuralization

ABSTRACT

The realization of artificial photosynthesis in the photocatalytic CO_2 transformation into valuable chemicals or solar fuels, such as CO, CH_4, HCOOH, and CH_3OH, by solar-light harvesting is a promising solution to both global-warming and energy-supply issues. Recently, zinc oxide (ZnO) has emerged as an excellent oxidative photocatalyst among non-titanium metal oxides due to its availability, outstanding semiconducting and optical properties, non-toxicity, affordability, and ease of synthesis. However, ZnO wide bandgap and inability to absorb in the visible region has demanded particular modification for its practical use as a sustainable photocatalyst. This review provides a panorama of the latest advancement on ZnO photocatalysis for CO_2 reduction with an overview of fundamental aspects. Various modification strategies such as transition metal and non-metal doping, loading of plasmonic metals, and surface vacancy engineering for tunning the properties and improving the performance of ZnO are elaborated. Composites or hetero-structuralization-based Z-scheme formation is also presented along with a detailed photocatalytic reduction mechanism. Moreover, a new novel Step-scheme (S-scheme) heterostructure modification with a charge transfer pathway mechanism is also highlighted. Finally, the key challenges and new directions in this field are proposed to provide a new vision for further improvement for ZnO-based photocatalytic CO_2 conversion.

1. Introduction

The recent fast-paced growth in the industrialized and global economy has contributed to energy shortage and environmental pollution. Besides, the excessive burning of fossil fuels results in a continuous rise in the concentration of CO_2, which consequently global warming. Almost 80% of global energy demands are met by the combustion of non-renewable fossil fuels, such as diesel, coal, and natural gas (Raizada et al., 2020). The sharp increase in CO_2 concentration in the atmosphere, *i.e.,* approximately from 280 ppm in early 1750 to 410 ppm in 2019, demands an indispensable need to reduce CO_2 *via* photochemical or electrochemical path (Fig. 1a) (Yang et al., 2019b). The latest Mauna Loa Observatory report in Hawaii that in the last ten years, the current CO_2 concentration in the atmosphere has reached up to 410 ppm

Abbreviations: Semiconductor, SC; conduction band, CB; carbon dots, CDs; density functional theory, DFT; dimethylformamide, DMF; 5,5-dimethyl-1-pyrolline-N-oxide, DMPO; density of states, DOS; diffuse reflectance spectrum, DRS; energy dispersive X-ray diffraction, EDX; electron-hole pairs, EHP; electron impedance spectroscopy, EIS; electron paramagnetic resonance, EPR; electron spin resonance, ESR; finite difference time domain, FDTD; fourier transform infrared, FTIR; internal electric field, IEF; lower unoccupied molecular orbital, LUMO; normal hydrogen electrode, NHE; nanoplates, NP; nanoparticles, NPs; nanorods, NR; oxidative photocatalyst, OP; photoluminescence, PL; reductive photocatalyst, RP; selected area electron diffraction, SAED; scanning electron microscopy, SEM; surface plasmon resonance, SPR; transmission electron microscopy, TEM; valence band, VB; X-ray diffraction, XRD; zeolitic imidazolate framework, ZIFs; Zinc Oxide, ZnO.

* Corresponding author.
** Corresponding author.
E-mail addresses: pankajchem1@gmail.com (P. Raizada), nguyenletridang@tdtu.edu.vn (D. Le Tri Nguyen), nvhuy@bdu.edu.vn (V.-H. Nguyen).

(Fig. 1b) (Singh et al., 2020). In the foreseeable future, fossil fuels can be replaced using renewable and alternative resources like water, radioactive, wind, and solar energy, which do not increase the atmospheric CO_2 level.

CO_2 is a relatively inert and stable molecule ($\Delta_f G^o_{298} = -394.36$ kJ mol^{-1}) with linear-configured C═O double bond energy, *i.e.,* 804.4 kJ mol^{-1}, that requires sufficient energy and the catalyst for its conversion into valuable chemicals (Kumar et al., 2021). Recent research reports suggest four main approaches related to CO_2 reduction, *i.e.,* hydrothermal conversion, thermal reforming, chemical transformation, and electrochemical conversion (Osterloh, 2017; Patial et al., 2020b; Sakakura et al., 2007). However, most of these routes are accompanied by some significant limitations: high costs, low efficiency, instability, and over-consumption of fossil fuel energy sources in the breakage of the C═O bond (Patial et al., 2020b; Samarghandi et al., 2020). Moreover, the low conversion efficiency for CO_2 reduction reaction with H_2O is obtained due to uphill reaction processes ($\Delta G > 0$) that require high activation energy.

As solar energy is the primary renewable energy source on the earth, the only way to end human life dependence on fossil fuels and reduce the impact of fossil fuel combustion on the environment is to attain energy from the sun. By mimicking natural photosynthesis, which involves H_2O, CO_2, and sunlight to form oxygen and carbohydrates, artificial photosynthesis is proposed as an alternative way of high solar energy conversion effectiveness (Majumdar et al., 2017; Singh et al., 2014; Zhu and Wang, 2017). To potentially solve the problems mentioned above, photocatalytic conversion of CO_2 to H_2O using solar energy and semiconductor (SC) photocatalyst into solar fuels, *i.e.,* methanol (CH_3OH), ethanol (C_2H_5OH), and hydrocarbons are considered as a sustainable approach, also known as artificial photosynthesis. This practice is adequate to address both global energy shortage and environmental issues without emitting CO_2 due to the following advantages:

i. Pollution-free and inexhaustible solar energy is utilized in the reaction procedure (Shokoohi et al., 2020; Sudhaik et al., 2020).
ii. Conversion reaction occurs mainly at ambient conditions: atmospheric pressure and room temperature (Kumar et al., 2020a,b,c; Rahmani et al., 2020).
iii. Abundantly available CO_2 and H_2O are used as initial reactants to produce hydrocarbon fuels (Karmee et al., 2010).
iv. Inert molecules are conversed into sustainable solar fuels without any secondary pollution (Shokoohi et al., 2020; Xu et al., 2015).

Therefore, photoreduction of CO_2 has been regarded as a "killing two birds with one stone" route to simultaneously save global energy and environmental issues (Won et al., 2015; Xi et al., 2012). In 1978, the work on photoelectrochemical reduction of CO_2 over p-GaAs under applied cathodic bias was conducted by Halmann and co-workers (Halmann, 1978). In the preceding year, Inoue et al. pioneered the photo-electrocatalytic CO_2 reduction into organic compounds, *i.e.,* methanol and formaldehyde, in CO_2-saturated aqueous solution of many semiconductors, such as CdS, TiO_2, ZnO, SiC, and GaP, under Xe-lamp illumination (Inoue et al., 1979).

A variety of materials ranging from titanium oxide (TiO_2) to non-titanium metal-based like WO_3, Cds, ZnO, $NaNbO_3$, $ZnGa_2O_4$, inorganic perovskite halide ($CsPbBr_3$), metal chalcogenides, MXenes (Ti_3C_2), metal-free materials, and metal-organic frameworks have been widely investigated as photocatalyst (Pare et al., 2009; Albero et al., 2020; Patial et al., 2020a; Raizada et al., 2020d). Fig. 2 represents the bandgap of some typical SC relative to the redox potential of specific possible products at pH 7 (Dutta et al., 2020; Nguyen et al., 2020; Raizada et al., 2020b). Among various non-titanium metal-based SCs, zinc oxide (ZnO) has been extensively used in photocatalysts for the photoreduction of CO_2 due to its unique photocatalytic properties. In particular, modified ZnO based photocatalyst for CO_2 reduction has become the hottest topic, and their evolution pathway with different modification is given in Fig. 3 (Deng et al., 2021; Fox, 1983; Núñez et al., 2013; Subrahmanyam et al., 1999; Yahaya et al., 2004; Yu et al., 2015).

Although several excellent reviews are covering the design, synthesis, and application of photocatalytic ZnO materials in the photocatalytic process, no such review in the field of CO_2 reduction is yet reported. Taken together, the development in CO_2 mitigation essentially profits from the progress of modified ZnO photocatalysts. Fig. 4a represents the percentage sharing of each strategy with modified ZnO using different keywords through the "Scopus" database. This comprehensive overview of photocatalytic modified ZnO covers the basic principle of CO_2 reduction, fundamental aspects of CO_2 adsorption, and activation

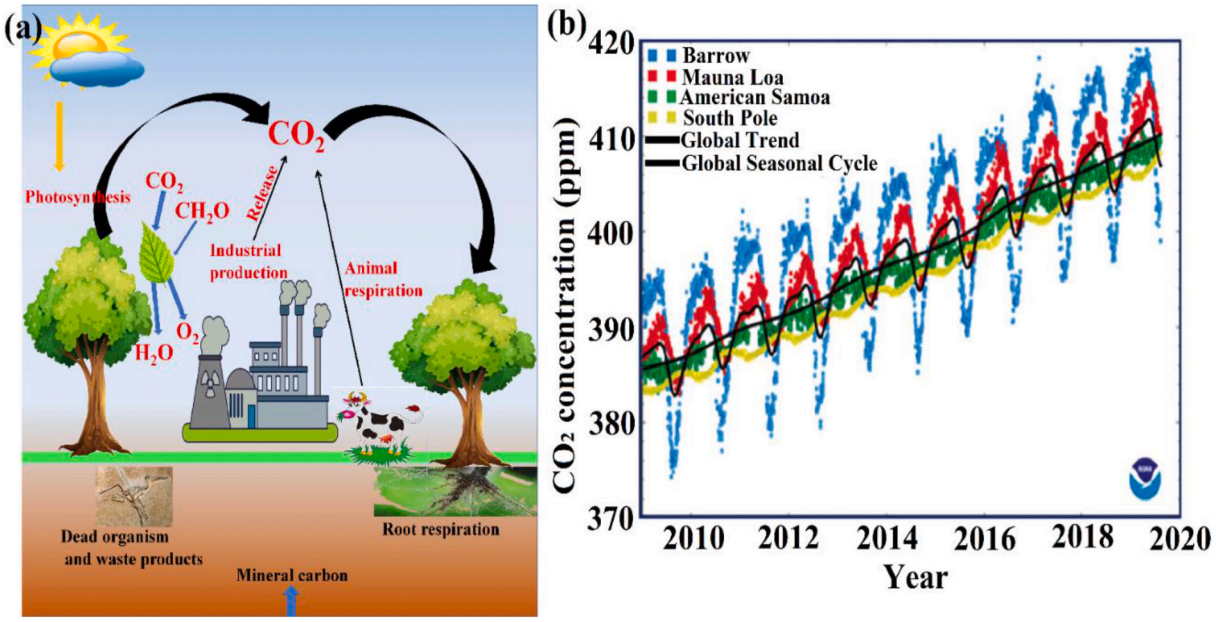

Fig. 1. (a) Pictorial representation of human caused carbon cycle, **(b)** Global tendency for the rise in CO_2 amount in the last ten years measured at distinct laboratories confined in the global monitoring divisions (GMD) of the Earth System Research Laboratory (ESRL). Reproduced with permission from Ref. (Singh et al., 2020). Copyright 2020 Royal society of Chemistry.

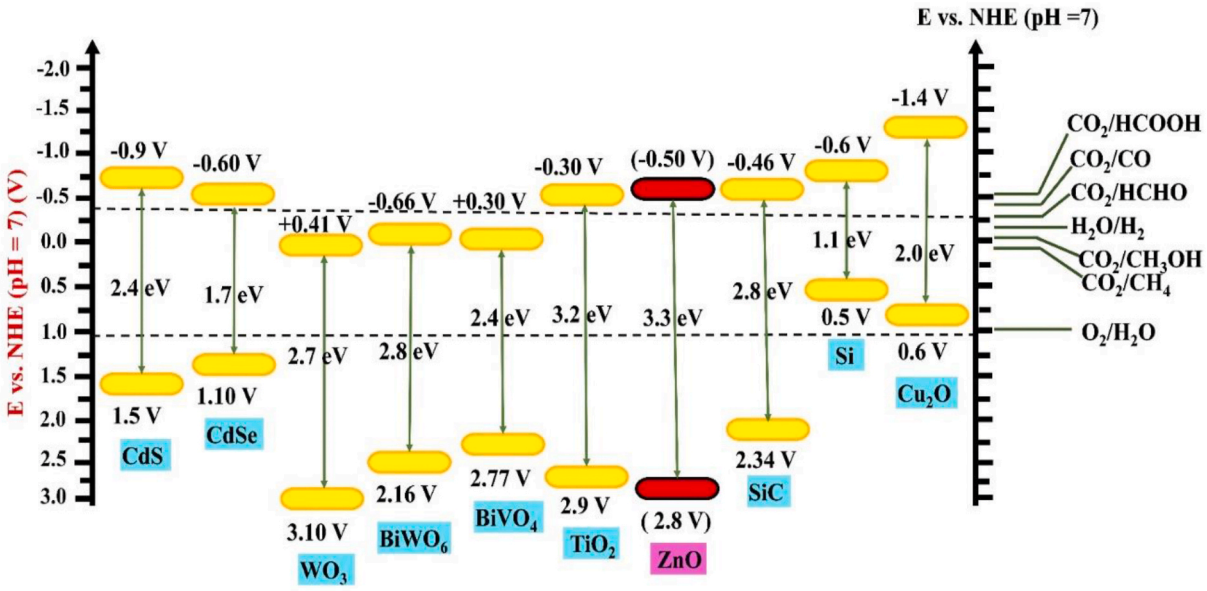

Fig. 2. Band structures of wide-variety of semiconductors with respect to the redox potentials of different products at pH = 7.

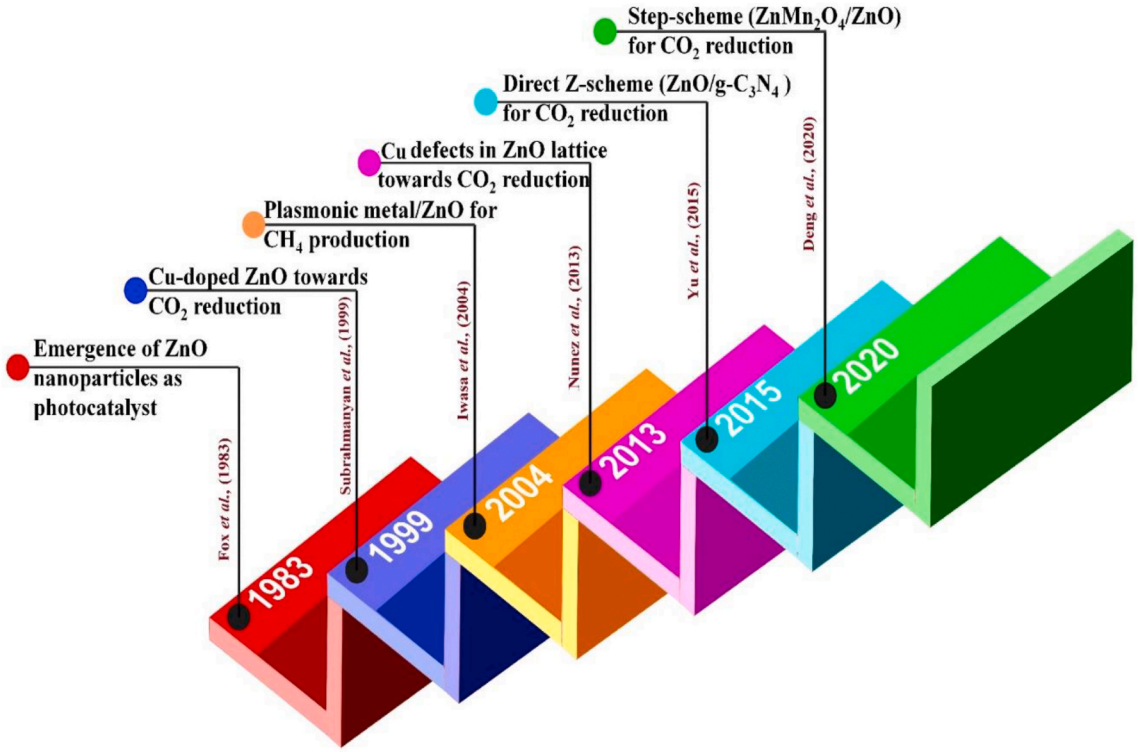

Fig. 3. The evolution pathway of the design and modification of the pristine ZnO.

with a brief discussion on the current advanced mechanism. The significant number of publications on "ZnO photocatalyst + CO_2 reduction" in the "Scopus" database ensures the popularity of this material owing to its remarkably excellent physiochemical and electronic properties as presented in (Fig. 4b and c). Pristine ZnO exhibits drawbacks of wide bandgap, low solar-light harvesting, deficient photo, and chemical stability, demanding specific strategies to overcome these limitations. The developed modifications for engineering ZnO structure are systematically summarized, including transition metal cation and non-metal anion doping, surface vacancy engineering, and plasmonic metal loading Z-scheme/S-scheme based hetero-structuralization. Lastly, challenges and future perspectives in photocatalytic CO_2 conversion are proposed, aiming to provide an overview of potentially modified ZnO photocatalyst to attain superior photocatalytic CO_2 capture and reduction.

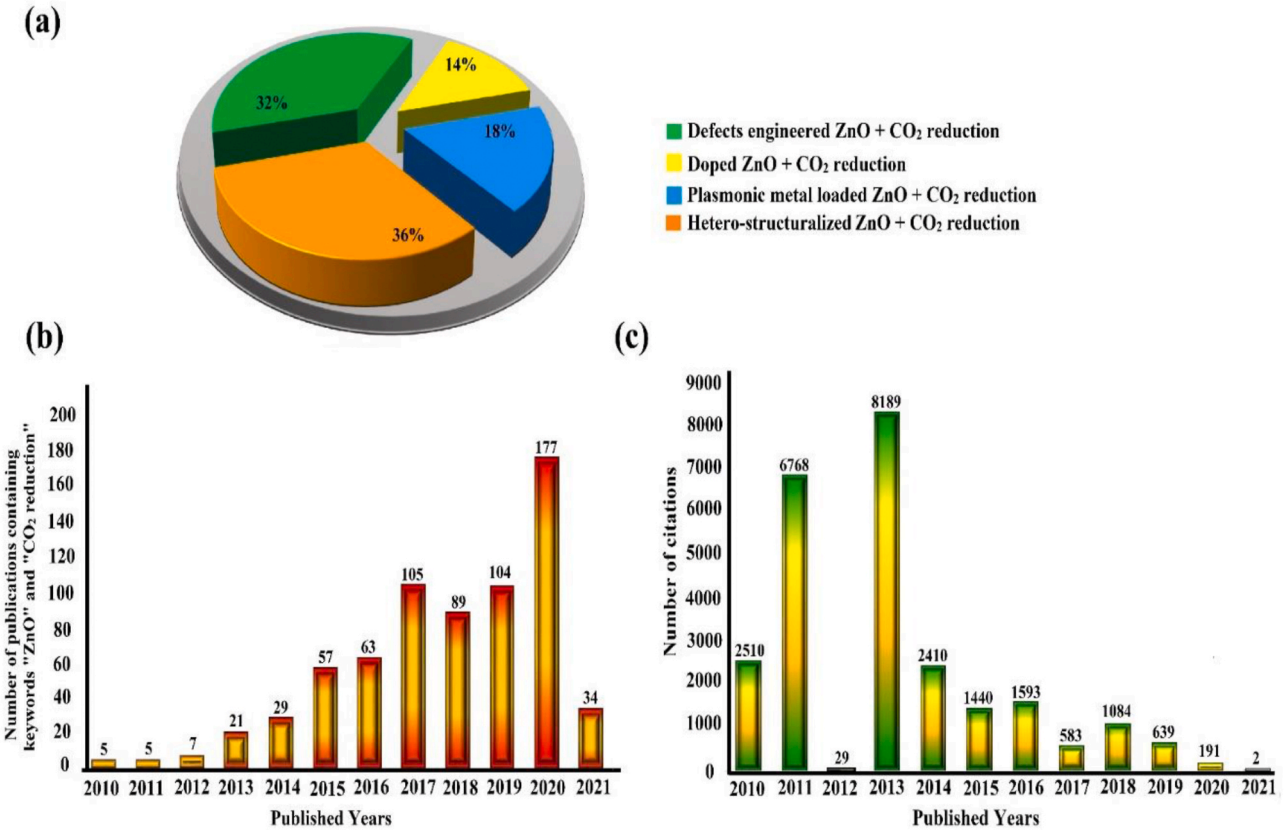

Fig. 4. Scopus literature analysis: (a) Various modification strategies of modified ZnO-based photocatalyst, **(b)** number of publications found by using keywords "ZnO and CO_2 reduction', **(c)** number of citations found by using keywords "ZnO and CO_2 reduction".

2. Theoretical basis of CO_2 photoreduction

2.1. Basic principle

Solar-light-driven photoassisted conversion of CO_2 into renewable fuels with water has gained significant attention since the discovery by Fujishima (Fujishima et al., 1979). The basic process of photoreduction of CO_2 involves three critical steps (Fig. 5):

i. Absorption of incident photons by SC with the same energy or greater than the bandgap energy and produces photoexcited electron-hole pairs (EHP). It is important to capture most of

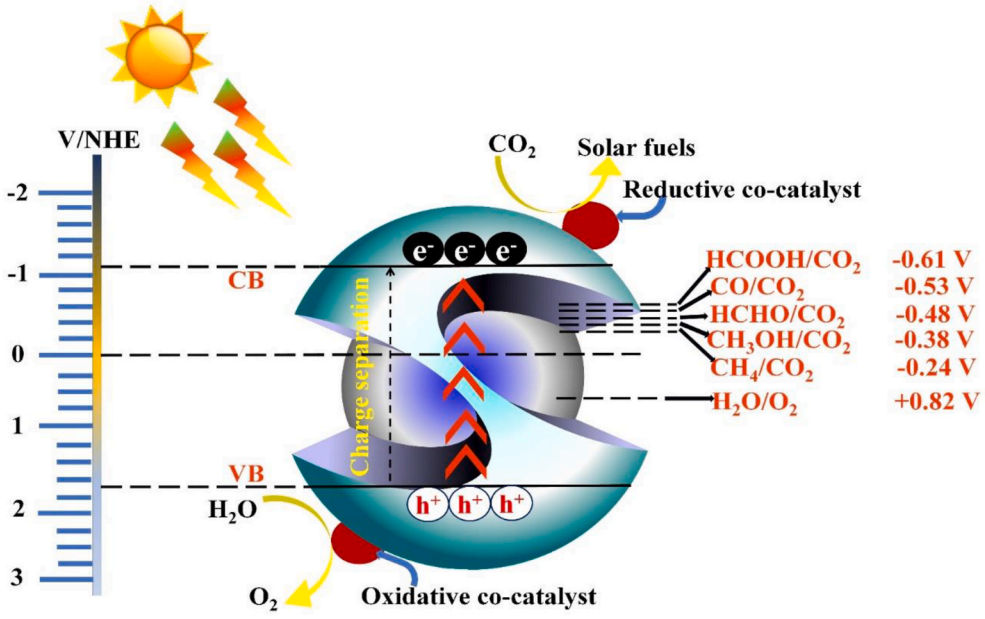

Fig. 5. Schematic representation of the overall reaction process for photocatalytic CO_2 conversion into thermodynamic parameters (CO, CH_3OH, CH_4, HCHO, HCOOH) with H_2O over a semiconductor photocatalyst.

visible and infrared light, which represent about 95% of the solar spectrum (Chen et al., 2012; Li et al., 2005; Shi et al., 2017; Thakur et al., 2020; Yang et al., 2019a).

ii. Migration and separation of charge carriers during the migration of charge carriers, many charges might be consumed by the recombination process. To make full use of photoexcited electrons and enhance charge separation, rational engineering of active sites like vacancy creation, cocatalyst doping, and facet-designing, is opted.

iii. The occurrence of a chemical reaction between surface-adsorbed species and charge carriers initiates CO_2 reduction (Kumar et al., 2020a,b,c; Leitner, 1996; Raizada et al., 2020e; Sharma et al., 2020; Thakur et al., 2020). Lastly, successive reduction reaction requires adsorption of CO_2 molecule at the active sites of SC. When the CO_2 molecule is adsorbed on the SC surface, it simultaneously acts as an electron acceptor or donor. Preferably, the redox potential of acceptor molecules must be more positive (lower in energy) than the conduction band (CB) edges of SC, and donor molecules should have redox potentials more negative (greater in energy) than the valence band (VB) of SC (Kumar et al., 2020a,b,c; Sharma et al., 2020).

Thus, band gap energy and redox potentials are two main criteria for electrons stimulation in the photoreduction of CO_2. A photocatalyst with an appropriate band structure is required for photoexcitation and transference of electrons to CO_2 to achieve the CO_2 reduction process under solar light. However, single-electron reduction of CO_2 is thermodynamically unfavourable due to more negative redox potential of $CO_2/CO_2^{\cdot-}$ *i.e.,* −1.85 V (vs. Normal Hydrogen Electrode (NHE), pH 7). Since CO_2 reduction is generally performed in aqueous media, the proton-assisted multi-electron reduction steps of CO_2 reduction are highly favorable by considering relative electrochemical redox potentials E° (V vs. NHE). The electrons from SC have more negative redox potentials for CO_2 transformation into hydrocarbons than photocatalytic water splitting reactions, as shown in (Fig. 6) (Bo et al., 2020).

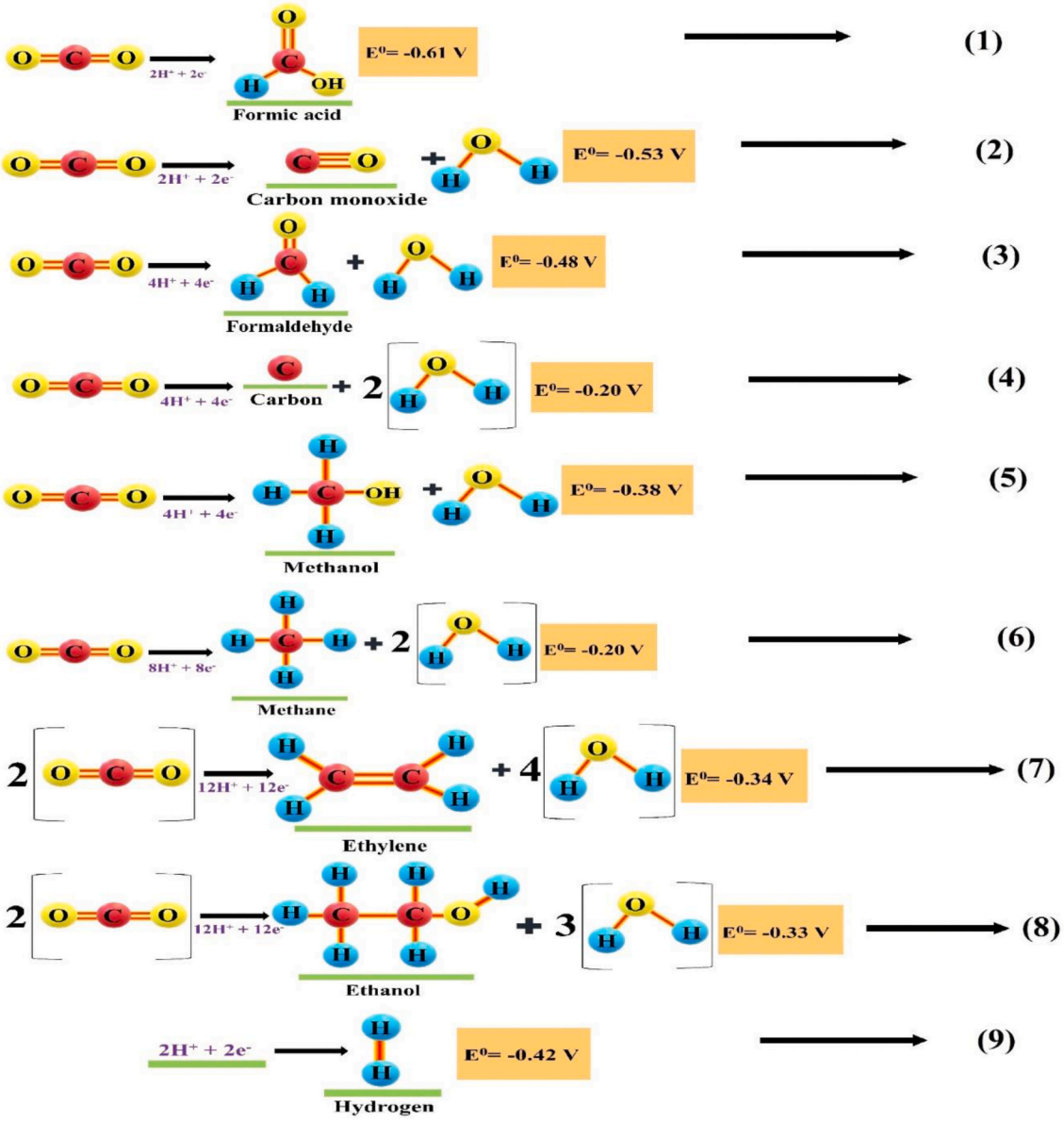

Fig. 6. Common electrochemical redox potentials for photocatalytic CO_2 conversion with corresponding reduction potentials (V vs NHE at pH = 7). Adapted with permission from Ref. (Bo et al., 2020), copyright 2020 Royal society of Chemistry.

2.2. CO_2 adsorption and activation aspects

The CO_2 adsorption and its activation on an SC surface are crucial and fascinating for CO_2 photoreduction. Both CO_2 activation and adsorption influence the successive reduction reaction and suppression of adjacent hydrogen evolution reaction. The chemical reaction between adsorbed CO_2 molecule and surface atoms leads to the generation of partially charged species $CO_2^{\delta-}$ (Fu et al., 2020). Three possible coordination schemes for CO_2 molecule, including oxygen coordination, carbon coordination, and mixed coordination, were proposed on the surface.

i. Each oxygen atom in CO_2 can donate lone pairs of electrons to lewis acid sites (Fig. 7a).
ii. The positively charged carbon atom could also gain electrons from lewis base sites like oxide ions to produce a carbonate-like structure (Fig. 7b).
iii. Both carbon and oxygen atoms in the CO_2 molecule can simultaneously behave as electron donors and acceptors, resulting in a mixed coordination species (Fig. 7c).

The adsorption amount of CO_2 molecules on the surface of the photocatalyst is known to be a selective-controlling and rate-determining step during the photoreduction process. To transform linear CO_2 into bent CO_2^{-} radical anion, considerable energy, and surface decoration strategies are required. Generally, high surface area photocatalyst has the most active centres for surface CO_2 adsorption, which promotes the CO_2 reduction process.

i. Diversified morphological nanostructure photocatalyst was fabricated to create higher surface area like 0D nanoparticles (NPs), 1D nanorods (NR)/nanowires/nanotubes, 2D nanosheets, and their hierarchical micro/nanostructure (Chen et al., 2019; Sun et al., 2019).

ii. Engineering surface defects on the photocatalyst surface effectively facilitate CO_2 activation and adsorption. Mainly, an oxygen vacancy is the most active site on the SC surface to alter the chemical and electronic properties.

2.3. Mechanistic route of CO_2 reduction

The mechanism of CO_2 reduction is complicated due to the complex thermodynamic and multi-electron kinetics reaction process. CO_2 reduction simultaneously involves the transference of six/eight protons/electrons with C═O bond breakage and C–H formation. The photoreduction of CO_2 can is influenced by many factors such as structural conformation of photocatalyst and operating parameters such as pH, temperature, and pressure (Mori et al., 2012). In the proposed mechanism of CO_2 reduction, three reaction process involves, *i.e.,* carbene, hydrogenation, and glyoxal pathways, which are as follows:

i. In the carbene route, a proton reacts with CO_2^{-} to generate CO through C–O cleavage. CO is further reduced to carbon residue and then carbon radical (C·) from coordinating electron and proton stimulation. Furthermore, C· accepts protons to get reduced into methane (CH_4), CH_3·, and CH·. The reaction between CH_3· and hydroxyl (·OH) results in the production of CH_3OH (Shkrob et al., 2012).
ii. In the hydrogenation pathway, a proton attacks a CO_2^{-} giving formic acid (HCOOH), accompanied by dehydration of dihydroxyl methyl to yield formaldehyde (HCHO). CH_3OH and CH_4 are formed when HCHO is further reduced (Fresno et al., 2018).
iii. Finally, the glyoxal route is different from the other two steps where both oxidative and reductive reactions involved, following the order CH_4, CH_3·, CH_3OC·, $HOCCH_2$·, $HOCH_2COH$, HOCCOH, $HOCCH_3$, HC·O, and CO_2^{-} (Sun et al., 2018). It has been noted that the reaction mechanism pathway is specifically related to the adsorption mode of CO_2^{-} on the photocatalyst surface.

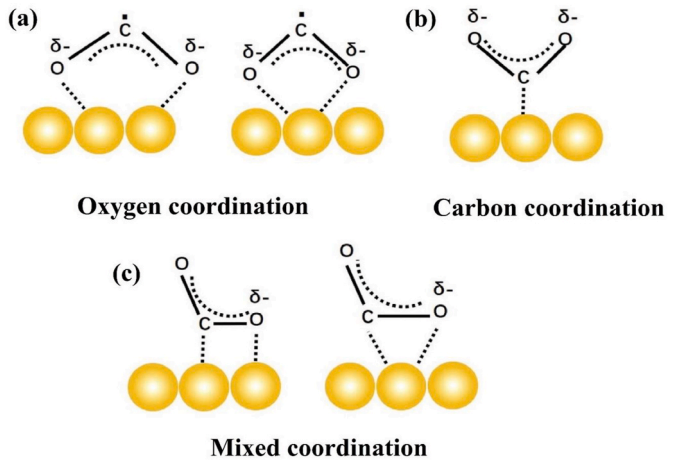

Fig. 7. The possible structure of adsorbed $CO_2^{\bullet-}$ on photocatalyst. Reproduced with permission from Ref. (Fu et al., 2020), copyright 2020 Elsevier.

3. ZnO as photocatalyst

The selection criteria of a photocatalyst with an appropriate bandgap towards CO_2 reduction is an essential factor that determines light absorptivity and charge carrier mobility. Accordingly, an appropriate photocatalyst for CO_2 reduction must accomplish the following demands:

i. Photoexcitation of maximum electrons from photocatalyst to CB;
ii. Highly negative CB potential of photocatalyst than the redox potential of CO_2 and reductive products;
iii. Reactants like H_2O, carbonate anion, or CO_2 must adsorb on the photocatalyst surface so that product yield could diffuse or desorb into the reaction after reduction steps of CO_2;

The addition of sacrificial agent or H_2O should be done to minimize the consumption of photogenerated holes at VB of photocatalyst, as shown in eq. (9) of scheme 1 (Habisreutinger et al., 2013). Thereby, among widely used non-titanium metal oxide, ZnO has been deemed a significant photocatalyst that fulfills all the properties mentioned earlier towards photocatalytic CO_2 reduction.

However, several SCs with wide band energy do not absorb the maximum amount of light. Among non-TiO_2 photocatalysts, ZnO is a promising SC on its wide bandgap (3.37 eV) with −0.50 eV CB and 2.80 eV VB edges, making it UV-active photocatalyst and high excitation binding energy at ambient temperature (60 meV). Compared to TiO_2, ZnO has drawn significant attention in photocatalysis due to its unique properties. These properties include earth-abundant and affordability, high charge stimulation potentials, feasible tunability, strong oxidation properties, safety and corrosion resistance, low cost, and maximum absorption efficiency across a large portion of the solar spectrum.

Initially, in 2004, Yahaya and co-researchers reported the comparative study among ZnO, TiO_2, and NiO towards photoreduction of CO_2 into CH_3OH using UV-laser light of 355 nm (Yahaya et al., 2004). NiO yields the maximum CH_3OH formation in 90 min, whereas using ZnO and TiO_2 decreased the yield of CH_3OH as a function of time increases showing the instability of product yield in the reaction process. For NiO, the amount of yield product increases while its rate of formation continuously decreases with time. This nature was explained through the successive reaction taking place between CH_3OH and H_2O with photogenerated holes. The photoactivity of pristine ZnO depends on microstructure, morphology, crystal size, and crystal orientation towards extended solar-light absorptivity enhanced EHP separation and

charge carrier mobility.

In terms of structural and electronic properties, ZnO commonly exists in rock salt, cubic (zinc blende), and wurtzite crystal structure, but at ambient conditions, the thermodynamically most stable structure is a wurtzite structure (Fig. 8a and b). The hexagonal wurtzite structure belongs to the space group (P_6mc) in the Hermann–Mauguin notation and atoms present crystallize in hexagonal unit cell forming close-pack lattice (Samadi et al., 2016). The ZnO primitive cell includes two formula units (black outlined), in which each sub-lattice comprises Zn^{2+} ions bounded by four O^{2-} ions and vice-versa, coordinated at the corners of a tetrahedron (Vogel et al., 1995). This tetrahedral coordination results in polar symmetry towards the hexagonal axis, piezoelectrical properties, which further induces defect formation and crystal growth. The wurtzite structure has been further categorized into four crystal faces of ZnO; including polar O-terminated (0001), Zn-terminated (0001) faces (along c-axis), and non-polar (1010), (1120) faces (along a-axis), both containing the same number of Zn and O atoms. The non-polar (1120) crystal face is less stable than both polar and non-polar (1010) faces. The two lattice parameters, a = 3.25 Å and c = 5.20 Å, in the ratio of c/a = 1.633, produce an ideal wurtzite crystal lattice. Recently, Radhakrishnan et al. reported the controllable synthesis of ZnO hexagonal cones, facet hexagonal NR, and hollow hexagonal NR with different ratios of (0001) facets by a feasible microwave-assisted wet-chemical method at different microwave temperature. The X-ray diffraction (XRD) resulted in an increased peak with a rise in microwave temperature of 700 °C per growth duration and decreased when cavities accumulated at ZnO's tips and converted into hollow. Besides, the selected area electron diffraction (SAED) and transmission electron microscopy (TEM) analysis confirmed the single crystalline nature with (0001) crystal facet along the c-axis. This is further supported by density functional theory (DFT) (Mohamad et al., 2017). As shown in (Fig. 8c), an energy band gap of pristine ZnO obtained from local density approximation without any spin-orbital interaction has been oriented along different symmetrical lines. The symmetrical lines in the Brillouin zone included of H (−0.3, 0.5, 0.7), L (0.0, 0.5, 0.5), M (0.0, 0.5, 0.0), G (0.0, 0.0, 0.0), K (−0.3, 0.0, 0.7), H (−0.3, 0.7, 0.5), A (0.0, 0.0, 0.5), G (0.0, 0.0, 0.0). The Fermi level was lies at 0 V while below and above of this orbital were VB and CB edges, respectively. The top of the VB and bottom of CB positioned at the same k-point, signifying ZnO as direct bandgap SC. The calculated band energy was found to be 0.75, which was almost identical to the data calculated (0.73–0.76 eV) from DFT. The bandgap attained experimentally from this study was found to be 3.26 eV, which was greater than the calculated value due to the calculation error of Kohn-Sham DFT. However, these results did not change the precision in the other relative properties of the crystal structure (*i.e.,* the density of states (DOS) and band structure).

The DOS determines the electron distribution function in an energy level, and to illuminate the chemical interaction in ZnO, all atoms were calculated by total (TDOS). The Fermi level for ZnO was stated at 0 eV, while DOS has been positioned between energy levels from −25 to 25

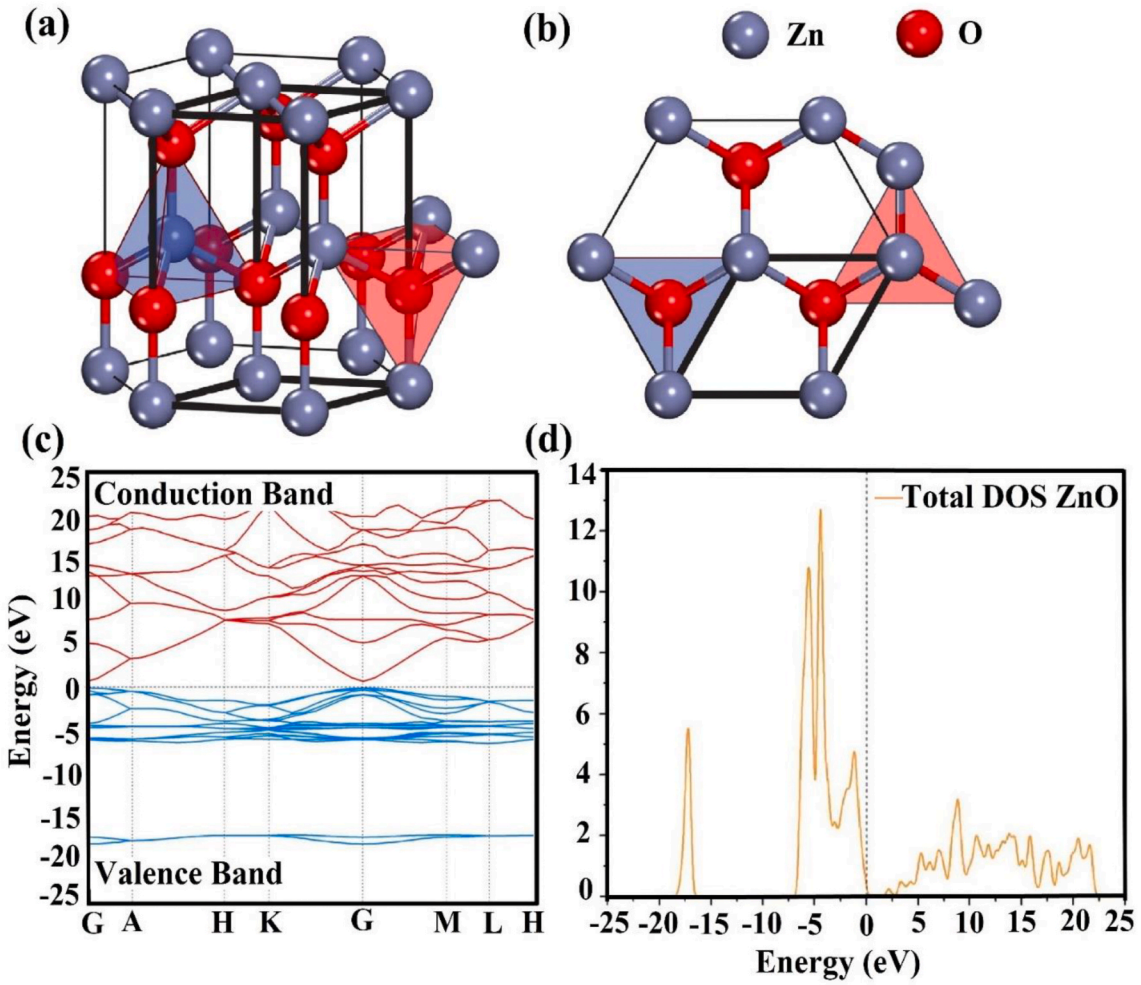

Fig. 8. Schematic view of ZnO wurtzite crystal structures **(a)** side view, **(b)** top view, **(c)** band energy assemblies of wurtzite ZnO showing conduction and valence band, and **(d)** total density of states (DOS). Reproduced with permission from Ref (Samadi et al., 2016; Mohamad et al., 2017). under license number 4978591406457, copyright 2016 Elsevier.

eV. The partial DOS (PDOS) state of the Zn atom was contributed by Zn 3d and Zn 4s and mainly positioned in the VB at −4.47 eV and 8.64 eV above the Fermi level. In contrast, PDOS of O atom in the VB band was mainly attributed by O 2p than O 2s because it located at −1.26 eV, which was nearer to the fermi level than O 2s at −17.25 eV. The contribution of all the atoms in the electronic bands of ZnO indicated that the uppermost valence state in ZnO was accompanied by predominant Zn 3d; O 2p orbital while O 2s in the lower state. The most dominant state was Zn 4s, followed by O 2p in TDOS of ZnO containing Zn 4s, O 2p, Zn 3d, and O 2s state in the CB band, represented by a single curve (Fig. 8d).

Unfortunately, ZnO only shows UV light (wavelength less than 380 nm) activity because it has a high bandgap (3.37 eV), which implies that it is mostly inactive under the visible region (the largest part of the solar spectrum). Other noticeable drawbacks involved in the pristine ZnO are as follows:

i. Dissolution at acidic pH,
ii. Poor charge carrier mobility
iii. Photo-corrosive nature of alkaline solution under UV illumination,
iv. Rapid recombination rate of its photoinduced electron-hole pairs,
v. Competitive proton reduction to hydrogen and agglomeration (Kumar et al., 2020a,b,c; Raizada et al., 2020a; Raizada et al., 2020c).

Therefore, the limitations above could be optimizing through variant strategical approaches to obtain efficient photoreduction of CO_2, which have been discussed below.

4. Strategies to boost the photocatalytic CO_2 reduction over modified ZnO photocatalyst

Despite recent advances in ZnO-based photocatalyst towards CO_2 photoreduction, the overall solar light conversion efficiency is still restricted due to the limitations mentioned earlier. To achieve high activity and product selectivity in photocatalytic CO_2 conversion, it is imperative to construct definite and engineering active sites for facilitating the activation and adsorption of CO_2 molecules. To this end, modification strategies like doping, hetero-structuralization, surface modification, loading of plasmonic metals, and surface vacancy engineering have been developed (Fig. 9). In the following, an in-detailed discussion with the primary reaction mechanism of these modifications has enabled further enhancement in CO_2 conversion activity.

4.1. Doping

Element doping can induce changes to the electronic and crystal structure of the parent SC, which acquires changes to the bandgap. In 2001, Asahi et al., gave the first report on bandgap engineering by nitrogen doping in TiO_2, which initiated the interest in this research field (Morikawa et al., 2001). The imaginary electric field generated at the metal-SC interface *via* doping increased the number of photoinduced carriers. These charge-carriers further transport to the surface where the redox reaction process takes place (Lim et al., 2014). Modification by doping has proven to be a successful approach for further improvement in the efficiency of photocatalytic reactions.

4.1.1. Metal doping

Metal atom doping (mostly transition metal with plasmonic characteristics) could behave as an electron-trapping agent under an excited state, which results in improved charge transport and electron mobility (Singh et al., 2013). Doping with transition metal cations like Ni, Cu, Fe, *etc.,* enables the construction of energy-levels in the band energy structure that minimizes the bandgap energy and EHP recombination as well, producing redshift in the absorption spectrum.

Among all the transition metals used for doping in ZnO, such as Ni, Fe, Cu, *etc.,* copper (Cu) has been widely used in ZnO specifically for CO_2 photoreduction. This might be due to the very close proximity in ionic radii of Zn^{2+} (0.74 Å) and Cu^{2+} (0.73 Å), which induces easy penetration of Cu^{2+} ions into ZnO crystal structure (Basumallick, 2020). Cu^{2+} doping has shown prominent effects on the structural, electrical, physical, chemical, optical, and magnetic properties of pure ZnO (Xiao and Frauenheim, 2013). Particularly, Cu^{2+} ions doping reduces EHP recombination, minimizes bandgap, and generates vacancy in the crystal lattice. For instance, Cu^{2+} was successfully incorporated at the substitutional site of wurtzite structural ZnO with a 3.41 eV bandgap compared to Zn^{2+} using a feasible electrochemical route photocatalytic

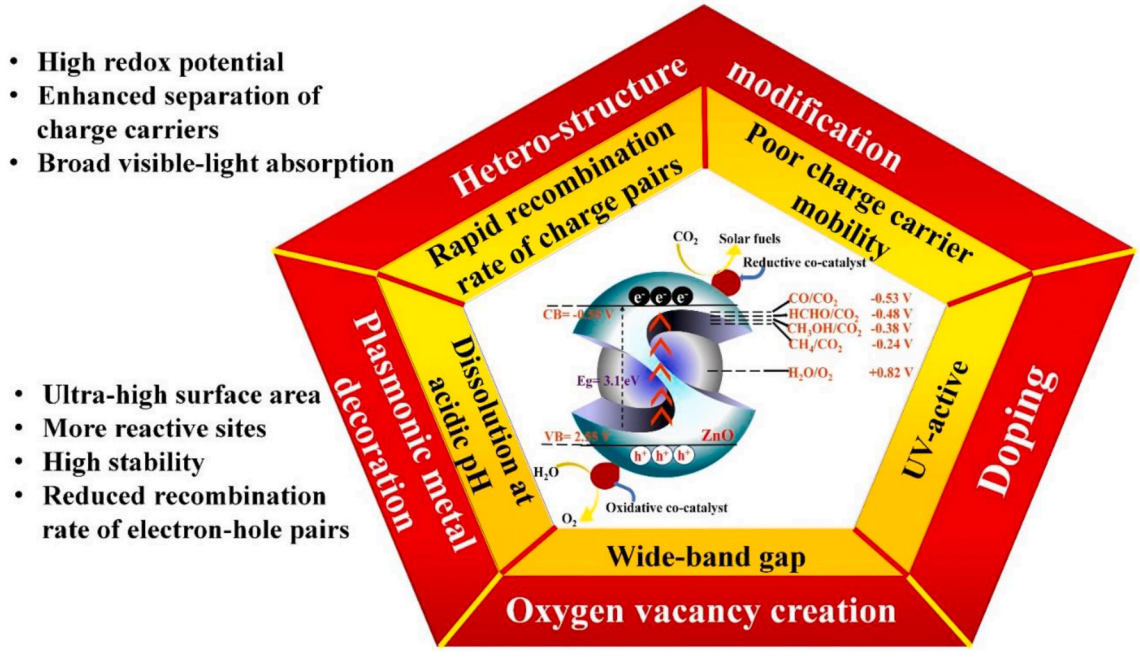

Fig. 9. Common electrochemical redox potentials required for CO_2 conversion with corresponding reduction potentials (V vs NHE at pH = 7).

CO_2 reduction (Ghahramanifard et al., 2018). Under visible-light irradiation, higher photocatalytic CO_2 reduction was possessed by 3.6% Cu-doped ZnO *i.e.,* 72.7% than 39.9% for 1.7% Cu-doped ZnO and 12.5% for bare ZnO. Photoluminescence (PL) results depicted that with Cu doping, the peak position at the UV region was shifted towards a higher wavelength (400–700 nm) with reduced intensity (Fig. 10a). A reduced bandgap of almost 3.2 eV was obtained for Cu-doped ZnO NR due to the strong hybridization of 3d and 2p orbitals between Cu and O, which shifted O2p upward. The lowest 3d energy level of ZnO CB was also occupied by substituting Cu^{2+}, resulting in a narrowing of the ZnO NR bandgap. From electron impedance spectroscopy (EIS) results, 1.7 and 3.6 %of Cu^{2+} doped ZnO displayed a negative slope for the Mott-Schottky plot showing substituted Cu ions acted as acceptors, which significantly enhanced charge carrier separation.

Furthermore, Garcia et al. reported the deposition of Cu ions onto bare ZnO (Cu–ZnO) using the ultrasonication method towards photocatalytic CO_2 reduction (Merino-Garcia et al., 2019). The photocatalytic activity of as-prepared Cu–ZnO photocatalyst was highest for CO_2 conversion into ethylene (C_2H_4), *i.e.,* 488 $\mu mol^{-2}\ s^{-1}$ than 14.3 and 3.5 $\mu mol^{-2}\ s^{-1}$ for CH_4 and CO, respectively. This remarkable improved reduction rate for C_2H_4 was two-fold more times than pure Cu NPs of 40–60 nm size (217 488 $\mu mol^{-2}\ s^{-1}$). In another work, Cu and Ni-doped ZnO were fabricated using a feasible nital-solution process at a low temperature of 180 °C using Zn $(CH_3COO)_2.2H_2O$, Ni $(NO_3)_2.6H_2O$ and Cu $(NO_3)_2.3H_2O$ as chemicals (Huerta-Flores et al., 2019). The doping of Ni^{2+} and Cu^{2+}transition metal ions in ZnO lattice induced oxygen vacancies by the destruction of a crystalline structure due to difference in ionic radie of (74 p.m.) Zn^{2+} than (71 p.m.) Cu^{2+} and (69 p.m.) Ni^{2+}. The photocatalytic CO_2 conversion into CH_3OH using ZnO-based photocatalyst was represented in the series as; ZnO (5 $\mu mol\ g^{-1}\ h^{-1}$) < Cu–ZnO (19 $\mu mol\ g^{-1}\ h^{-1}$) < Ni–ZnO (29 $\mu mol\ g^{-1}\ h^{-1}$). This improved reduction rate for Ni–ZnO was attributed due to maximum oxygen vacancy sites and intermediate levels which prolonged the time-span of charge carrier.

4.1.2. Non-metal doping

Doping with anions (B, C, N, S *etc.,*) is also a promising strategy that has been employed to boost the photocatalytic performance of ZnO by promoting charge carrier separation and broader light absorptivity. Cation doping usually produces additional effects or impurities in ZnO, which may act as recombination centres. In contrast, doping with non-metals with small radii are promising candidates because they easily substitute for lattice oxygen sites of ZnO or occupy interstitial sites. Due to its larger solubility in metal oxides and comparable size with oxygen, nitrogen is widely used as a dopant to modify the electronic structures of metal oxides as only small formation energy is required for the substitution process. For example, Oliveira et al. synthesized nitrogen-doped ZnO (N–ZnO) *via* the polymeric precursor method using zinc acetate and urea as precursors (Oliveira et al., 2018). The partial substitution of N in O induced change in ZnO crystallinity, resulting in effective photocatalytic CO_2 reduction because of existing exposed active sites during reduction reactions. These exposed active centres increased the structural defects, which further improved charge-kinetics reactions. Under UV–visible light illumination (254–400 nm), the maximum CH_4 production rate (0.21 mol $L^{-1}g^{-1}h^{-1}$) was achieved by 2 wt%N–ZnO photocatalyst under 24 h of reaction time in the NaOH solution at 450 °C.

In another work, visible-light-driven ZnO NR photocatalyst with distinct bimodal carbon amendment (both carbon decoration and loading) (C–ZnO) were prepared using zeolitic imidazolate framework (ZIFs)-8 polyhedral precursor *via* calcination technique at 400 °C (Liu et al., 2016). Here, decoration with C improved the free-carrier movement and inhibited the photocorrosion, while C doping increased optical absorption in the visible region. Further, the nitrogen adsorption isotherm results revealed that the ultra-high surface area (1008 m^2g^{-1}) and mesoporous structure (2.62 nm pore size) was partly inherited from extremely flexible porous ZIFs-8 frameworks at 300 °C calcining temperature (Fig. 10b and c). The C–ZnO photocatalyst (at 500 °C) delivered 6 times higher CH_3OH production rate, *i.e.,* 0.83 mmol $g^{-1}\ h^{-1}$ than ZnO NR (0.14 mmol $g^{-1}\ h^{-1}$) with 40 m^2g^{-1} surface area and 0.20 mmol g^{-1} CO_2 uptake. Hence, the effective CO_2 photoreduction activity was attributed to bimodal carbon alteration, crystalline porous framework, and ultrahigh surface area, which facilitated the CO_2 capture, charge-transfer, and promoted visible-light absorption.

4.2. Oxygen vacancy creation

The presence of oxygen vacancies in the ZnO lattice promotes the light-absorptivity in the visible-light range and serves as activation sites for CO_2 molecules. Oxygen vacancy introduction inside the ZnO lattice (a kind of intrinsic n-type defect) generally prevents p-type ZnO formation (Wu et al., 2018b). These vacancies' significant advantages are the narrowest of wide bandgap, reduced EHP recombination, high thermal conductivity, and carrier concentration. Hydrogen plasma treatment was found very useful in improving the electrical and optical properties of the ZnO. For instance, ZnO nanosheets with co-exposed (0002) and (1120) facets were synthesized by H_2 plasma treatment for

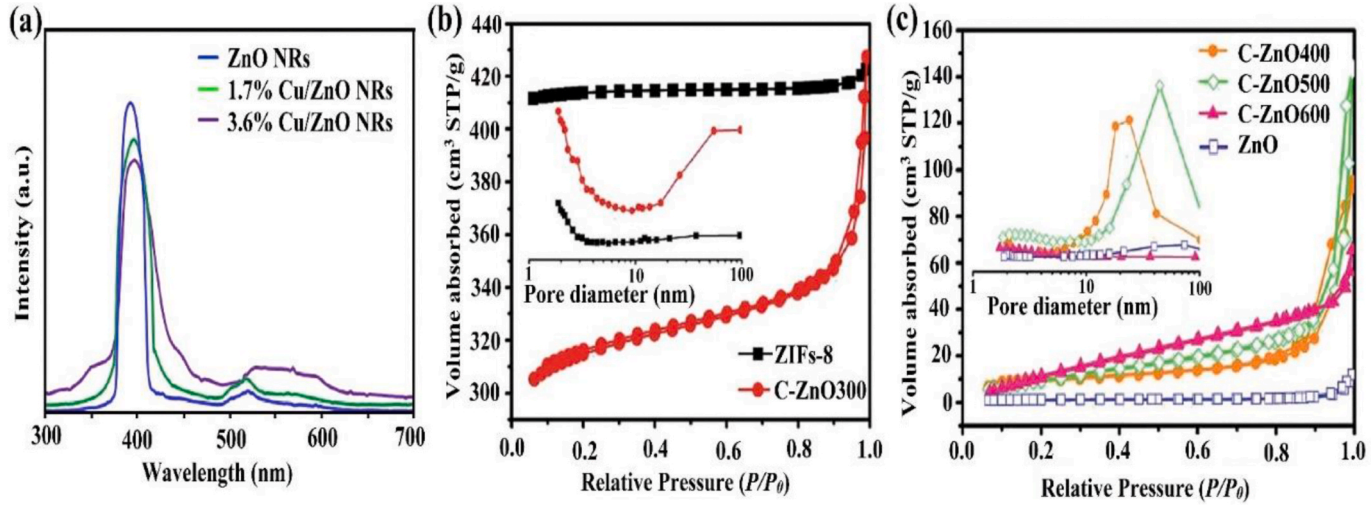

Fig. 10. (a) PL spectra of bare and Cu-doped ZnO with different amount of Cu dopant, **(b)** N_2 adsorption isotherm and their consistent pore sizes distribution curves (inset) for the ZIFs-8 and C–ZnO300 photocatalyst, in comparison to C–ZnO400, C–ZnO500, C–ZnO600, and pure ZnO **(c).** Reproduced with permission from Ref (Ghahramanifard et al., 2018; Liu et al., 2016). under license number 4978591406457, copyright 2016 Elsevier.

120 s and 30 s with oxygen-rich ZnO and oxygen-deficient ZnO nanosheets, respectively (Geng et al., 2018). From the density functional theory (DFT) study, the effects of oxygen vacancies on ZnO's structural properties were determined. As shown in (Fig. 11a and b), a new defect level was generated for the ZnO nanosheets with oxygen vacancies above the VB maximum. Also, the partial charge density resulted in the accumulation of electrons around the VB energy level of ZnO with an oxygen vacancy compared to oxygen-deficient ZnO nanosheets (Fig. 11c and d). These exposed electrons confined at the VB maximum were transported into the anti-bonding energy levels of CO_2 molecules used for CO_2 activation. The oxygen-rich ZnO photocatalyst possessed an optimum current density of -16.1 mA cm^{-2} for CO production, which was 1.4 and 5.1 times greater than oxygen-deficient ZnO and bare ZnO with faradaic efficacy of 83%. The overall photocatalytic reduction process into CO mainly involved the following reactions;

$$CO_2 + \# + e^- + H^+ \rightarrow COOH^* (Activation\ phenomenon) \quad (1)$$

$$COOH^{\#} + e^- + H^+ \rightarrow CO^* + H_2O\ (Surface\ adsorption) \quad (2)$$

$$CO^{\#} \rightarrow CO + \#(Desorption\ activity) \quad (3)$$

Oxygen vacancies in ZnO lattice could promote photocatalytic performance by producing defect levels that serve as trapping sites for photogenerated holes. Hegazy and co-researchers synthesized the ZnO NPs *via* thermal decomposition technique at 400 °C, 350 °C, and 300 °C (denoted as ZnO400, ZnO350, and ZnO300) using distinct liquid solutions for CO_2 conversion into CH_3OH and CH_3CHO (Hegazy et al., 2020). The existence of oxygen vacancy was confirmed by Fourier transform infrared (FTIR) and Raman spectroscopy. The peak intensity at 435.85 cm^{-1} of Raman spectra for all three samples represented the E_{2H} active mode, indicating the hexagonal wurtzite structure of ZnO. Besides, peaks positioned at 380.35 and 329.84 cm^{-1} were imputed to A_1(TO) and E_{2H}-E_{2L} multi-photon modes, respectively. However, the spotted signal at 574.58 cm^{-1} representing A_1 (LO) vibration confirmed the existence of oxygen vacancies in the ZnO crystal lattice (Fig. 12a). Also, FTIR analysis depicted the strong peak positioned at 500 cm^{-1} was attributed to oxygen vacancies in the ZnO crystal lattice, which was weaker in the case of ZnO350 than ZnO400 and ZnO300 (Fig. 12b). It was found that CH_3OH production decreased in the order of NaCl < NaOH < $NaHCO_3$ over ZnO350 sample. In the presence of $NaHCO_3$, the optimal ZnO350 displayed the maximum photoconversion of CO_2 to 113 $\mu molg^{-1}$ CH_3OH and 19.5 $\mu molg^{-1}$ CH_3CHO production rate than ZnO400 (5.3 $\mu molg^{-1}$ CH_3OH and 8 $\mu molg^{-1}$ CH_3CHO) and ZnO350 (52 $\mu molg^{-1}$ CH_3OH and 12.2 $\mu molg^{-1}$ CH_3CHO). Moreover, the proposed mechanism of charge transference and CO_2 photoreduction reactions was shown (Fig. 12c). Under UV light irradiation, the photoexcited e^- at VB of ZnO350 and ZnO300, when transported to the corresponding CB, were trapped by active oxygen centres resulting in increased photocatalytic activity. Here, the photocatalytic reduction activity reduced at 400 °C mainly due to abundant oxygen vacancies that act as recombination sites for photogenerated holes. Thus, the incorporated oxygen vacancies in the ZnO structure resulted in enhanced charge carrier stimulation than becoming recombination centres.

Recently, Li and co-researcher reported oxygen defects into porous

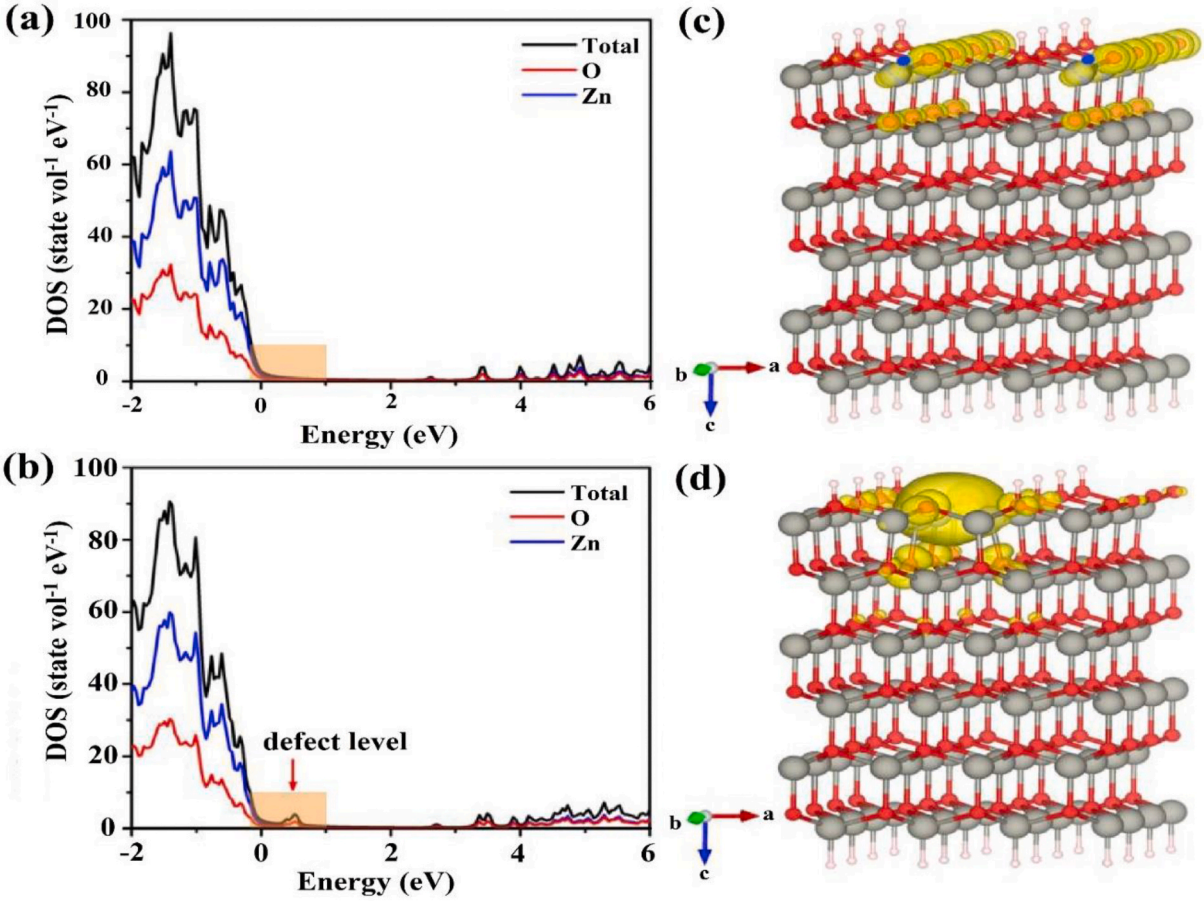

Fig. 11. DOS of (a) ZnO cluster, (b) oxygen-vacancy rich ZnO cluster. The partial charge density (orange region) of **(c)** ZnO cluster and oxygen-vacancy rich ZnO cluster with respect to valence band maximum. Here, Zn, H, and O atoms are represented by grey, white and red spheres, respectively, while yellow parts refer to charge density curve. Reproduced with permission from Ref (Geng et al., 2018). under license number 4978680043872, copyright 2018 Wiley. (For interpretation of the references to colour in this figure legend, the reader is referred to the Web version of this article.)

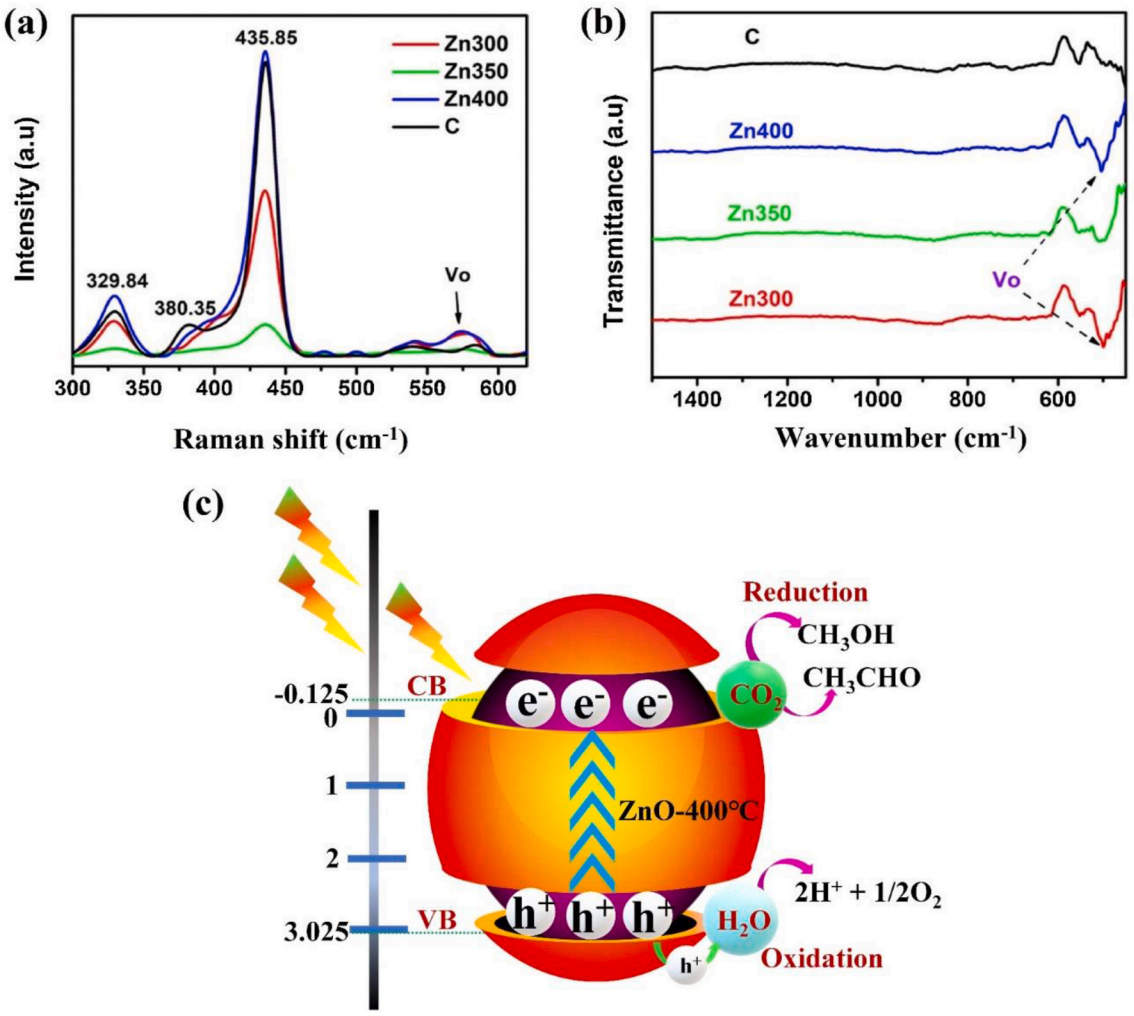

Fig. 12. (a) Raman spectra**, (b)** FTIR study of ZnO samples, and (c) reaction mechanism over ZnO-400 °C. Reproduced with permission from Ref (Hegazy et al., 2020). under license number 4979180505958, copyright 2020 Elsevier.

ZnO nanoplates (NP) *via* annealing ZnS (ethylenediamine) as precursors at specific temperatures, *i.e.,* 600, 650, and 700 °C (denoted as Zn600, Zn650, and Zn700) (Li et al., 2019). The two main factors for effective photoreduction of CO_2 by porous ZnO NP were CB potential and light-harvesting capacity. Thereby, the UV–visible light spectrum determined the bandgap of porous Zn600, Zn650, and Zn700 NP as 3.21, 3.24, and 3.25 eV, respectively. Besides, transmission electron microscopy (TEM) and energy-dispersive X-ray diffraction (EDX) spectra investigated the atomic ratios of O/Zn for Zn600, Zn650, and Zn700 as 0.65, 0.77, and 0.97, revealing the presence of oxygen vacancy while the defect amount decreased with increasing annealed temperature. The photocatalytic activity for CO_2 reduction into CO followed the increasing order of Zn600 > Zn650 > Zn700 with the production rate of 3.8, 3.1, and 2.5 $\mu molg^{-1}$, respectively. Thus, the Zn-600 NP exhibited the maximum separation efficacy and CO_2 adsorption capability among all samples.

Oxygen vacancies in ZnO can also be created by adding carbon dots (CDs), representing exceptional up-conversion photoluminescence (UCPL) feature and e^- transference capability. The photoreaction of CO_2 with H_2O vapor under light irradiation from UV–visible to near-infrared (NIR) range (λ = 250–950 nm) was evaluated over oxygen vacancy-rich ZnO/CDs nanocomposite. The ZnO/CDs sample was prepared in an aerosol furnace reaction at the different furnace temperature range from 500 to 650 °C. Under UV-visible-NIR illumination, the photocatalytic CO production rate of ZnO/CDs-N_2 sample at 600 °C 118.8 $\mu molg^{-1}h^{-1}$ with a quantum yield of 0.26%, which was 22.5 and 3.7 times greater than pristine TiO_2 (P25) (5.3 $\mu molg^{-1}h^{-}1$) and ZnO/CDs-Air composite at 550 °C (32.2 $\mu molg^{-1}h^{-1}$), respectively (Fig. 13a) (Lin et al., 2020). As shown in (Fig. 13b), the ZnO/CDs-N_2-600 °C possessed strong recyclability up to four successive cycles with only 14% decreased CO production rate ZnO/CDs-Air-550 °C displayed 60% decreased yield in CO_2 photoreduction. The decreased photoreduction activity was observed mainly due to the aggregation of carbon atoms at the vacant active sites on the surface of the photocatalyst. The band alignment and charge transference mechanism, along with the reaction route for CO_2 reduction, in addition to H_2O over ZnO/CDs-N_2-600 °C photocatalyst was given in (Fig. 13c). Under the visible-NIR region (λ = 400–950 nm), e^- transference takes place from the lower unoccupied molecular orbital (LUMO) of CDs-N_2-600 °C at −2.88 V to the −3.3 V CB of ZnO, thereby reducing EHP recombination and enhancing charge carrier stimulation. The high surface area of 79 m^2/g and hollow structure facilitates the transference and adsorption of CO_2 and H_2O molecules, which reacted with several adsorption active centres producing ·OH radicals and intermediate carbon products. The rich oxygen vacant sites enhanced the CO_2 adsorption by reducing the kinetic barrier, which induced the generation of HCOOH and CO_2^- groups on the surface of ZnO/CDs-N_2-600 °C photocatalyst. The CO_2^- and HCOOH species were readily converted into CO by taking maximum protons and e^- from dissociated H_2O and sufficient charge separation. Notably, in the proposed reaction mechanism, only one e^- was required to convert CO_2^- to

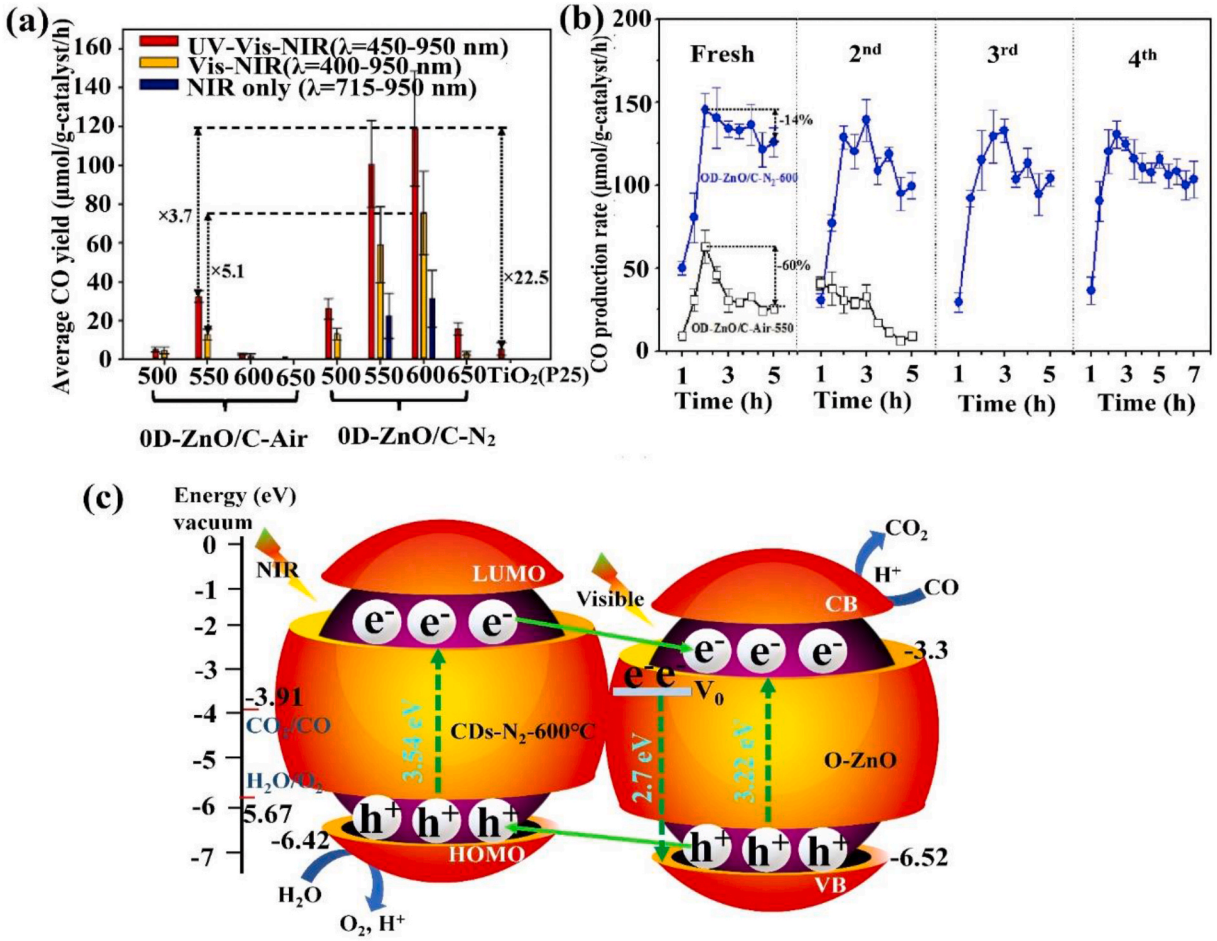

Fig. 13. (a) Typical CO yield over 0D-ZnO/CDs-Air, 0D-ZnO/CDs-N_2, and TiO_2(P25) under different absorption wavelength, **(b)** photocatalyst recyclability and stability test over 0D-ZnO/C-Air-550 °C and 0D-ZnO/CDs-N_2-600 °C up to four consecutive cycles, and **(c)** proposed reaction mechanism over O–ZnO/CDs-N_2-600 °C photocatalytic system. Reproduced with permission from Ref (Lin et al., 2020). under license number 4979190112235, copyright 2020 Elsevier.

CO under light illumination. Thus, the oxygen vacancies on the surface of the ZnO photocatalyst could offer new adsorption sites to CO_2 molecules.

4.3. *Plasmonic cocatalyst loaded ZnO*

Plasmonic metal NPs such as Ag and Au decorated on ZnO are expected to exhibit the following three properties:

i. **Migration and separation of photogenerated charge carriers for the development of Schottky barriers**: the promoting effect of plasmonic Au- and Ag-based cocatalyst for charge separation is based on Schottky junction. Decorating ZnO with Au NPs was an intriguing approach to passivate the prominent surface defects in ZnO through near-field plasmonic enhancement or light scattering (Narváez et al., 2019). For example, Zheng et al., prepared 3D plasmonic Au/ZnO photocatalyst with inverse-opal structure via in-situ growth on the outer and inner of ZnO lattice. This spatial charge transference route between Au NPs and ZnO Schottky junction significantly enhanced the EHP separation efficiency and visible-light absorption as well (Zheng et al., 2020).

ii. **Broader visible-light harvesting capacity and EHP excitation on the ZnO surface due to plasmonic energy transport from the plasmonic metal to the ZnO framework.** Recently, Au NS were decorated on ZnO NR, forming a 3D hetero-nanostructure *via* wet chemical and magnetron sputtering deposition at the glancing angle, which enhanced the visible-light absorption region. The hot e^- injection and generation process over Au/ZnO Schottky interface mediated by Au NS were responsible for the enhanced photoactive properties. The blue-shift peak of the surface plasmon absorption band between 450 and 1000 nm was observed as the thickness of the Au NS was increased up to 40 nm and due to strong interaction between Au NS and ZnO NR (Ghaemi-moghadam et al., 2021).

iii. **Modification in surface properties of ZnO framework by optimizing surface functionalization, morphology control and nanosizing engineering** (Iwantono et al., 2015; Solangi et al., 2011).

The molecular-level concept of the solar light-driven CO_2 reduction was well understood by designing high-efficiency plasmonic photocatalytic systems. For instance, Zhao and co-researchers reported the Pd, Au, and Ag NPs decorated with 3D porous ZnO NS, synthesized by the hydrothermal method using urea propylene oxide/ethylene oxide as a precursor, which catalyzed the CO_2 photoreduction (Fig. 14a) (Zhao et al., 2019). Among these metallic plasmons, Au NPs displayed maximum visible-light absorption (530 nm) and permitted direct decomposition of inert C–H bonds due to the presence of plasmon resonance energy hot injected e^-, exceptionally generating C_2 products, C_2H_6. A 10-fold (27.0 μmol g^{-1} h^{-1}) enhancement in the photocatalytic activity was observed, and 1.03% of quantum yield due to an internal electric field (IEF) formed by surface plasmon of Au NPs. The SEM results indicated the vertically aligned ultrathin NS (5.0 μm in size) of pure metal-ZnO shaped into an intertwined design (Fig. 14b). The thickness

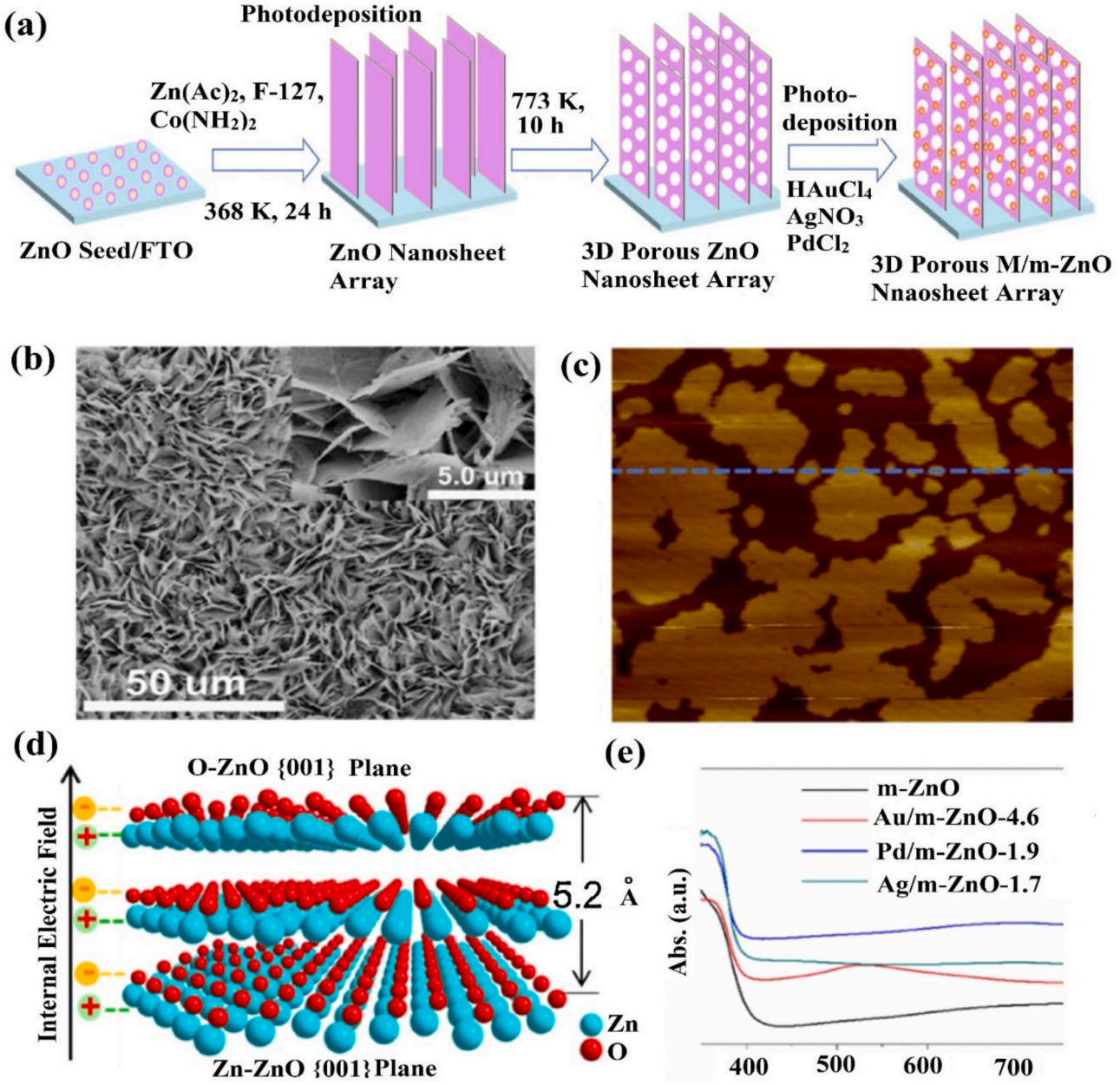

Fig. 14. (a) Diagrammatic synthesis procedure of plasmonic metals/3D porous-ZnO nanosheets array, **(b)** scanning electron microscopy (SEM) and **(c)** atomic force microscopy (AFM) image of 3D porous- ZnO nanosheets array, **(d)** crystal lattice and charge dispersion of porous ZnO nanosheet along the [001] facet, and **(e)** UV–vis diffuse reflectance spectra (DRS) of ZnO nanosheets array with different plasmonic metals. Reproduced with permission from Ref (Zhao et al., 2019). under license number 4979221398090, copyright 2019 Elsevier.

(~1.6 nm) of the NS parallel to the six layered-ZnO along (100) axis was evaluated from atomic force microscopy (AFM) analysis (Fig. 14c). The atomic layers of ZnO NS in the asymmetric pattern were getting aligned along the c-axis, forming an intense IEF between O-terminated ZnO (001) plane and Zn-terminated (001) plane, which enhanced the EHP separation efficiency (Fig. 14d). UV–visible diffuse reflection spectrum (DRS) results displayed the maximum light absorptivity for Au NPs/ZnO-4.6 mol% *i.e.,* 530 nm than Ag/ZnO-1.7 mol% and Pd/ZnO-1.9 mol% with *ca.* 395 nm absorption (Fig. 14e). Under solar-light illumination, the photocatalytic CH_4 production rate was highly achieved for Au/ZnO-4.6% *i.e.,* 21.0 μmol g^{-1} h^{-1}than Pd/ZnO-1.9% (18 μmol g^{-1} h^{-1}) while, Ag/ZnO-1.7% showed only CO production rate of 25 μmol g^{-1} h^{-1}.

In another work, Wang and co-workers reported plasmonic photo-excitation of Au on ZnO photocatalyst surface using 532 nm laser irradiation significantly induced the plasmonic heating of the photo-catalyst, yielding CO and CH_4 products from H_2 and CO_2 reactants (Wang et al., 2013). Scanning electron microscopy (SEM) results depicted that Au nanoparticle~20 nm was dispersed on the ZnO surface at a few particle densities/μm^2 (Fig. 15a). As shown in (Fig. 15b), the size of Au nanoparticles was reliable to diffuse reflectance spectra (DRS) of Au-doped ZnO, which confirmed the surface plasmonic resonance (SPR) effect of Au nanoparticle around 538 nm. Thereby, the plasmonic peak of Au-doped ZnO was in resonance with laser-induced excitation wavelength at 532 nm than pristine ZnO, which possessed no absorption of the visible-light region. After plasmonic heating of Au–ZnO under laser intensity of 8×10^5 W m^{-2} predominantly resulted in the photo-reduction of CO_2 into 4.22 μmol g^{-1} h^{-1} CO and 1.2 μmol g^{-1} h^{-1} CH_4 with 0.030% quantum yield. The SPR effect of Au NPs enhanced photocatalytic activity and increased recombination time, and improved

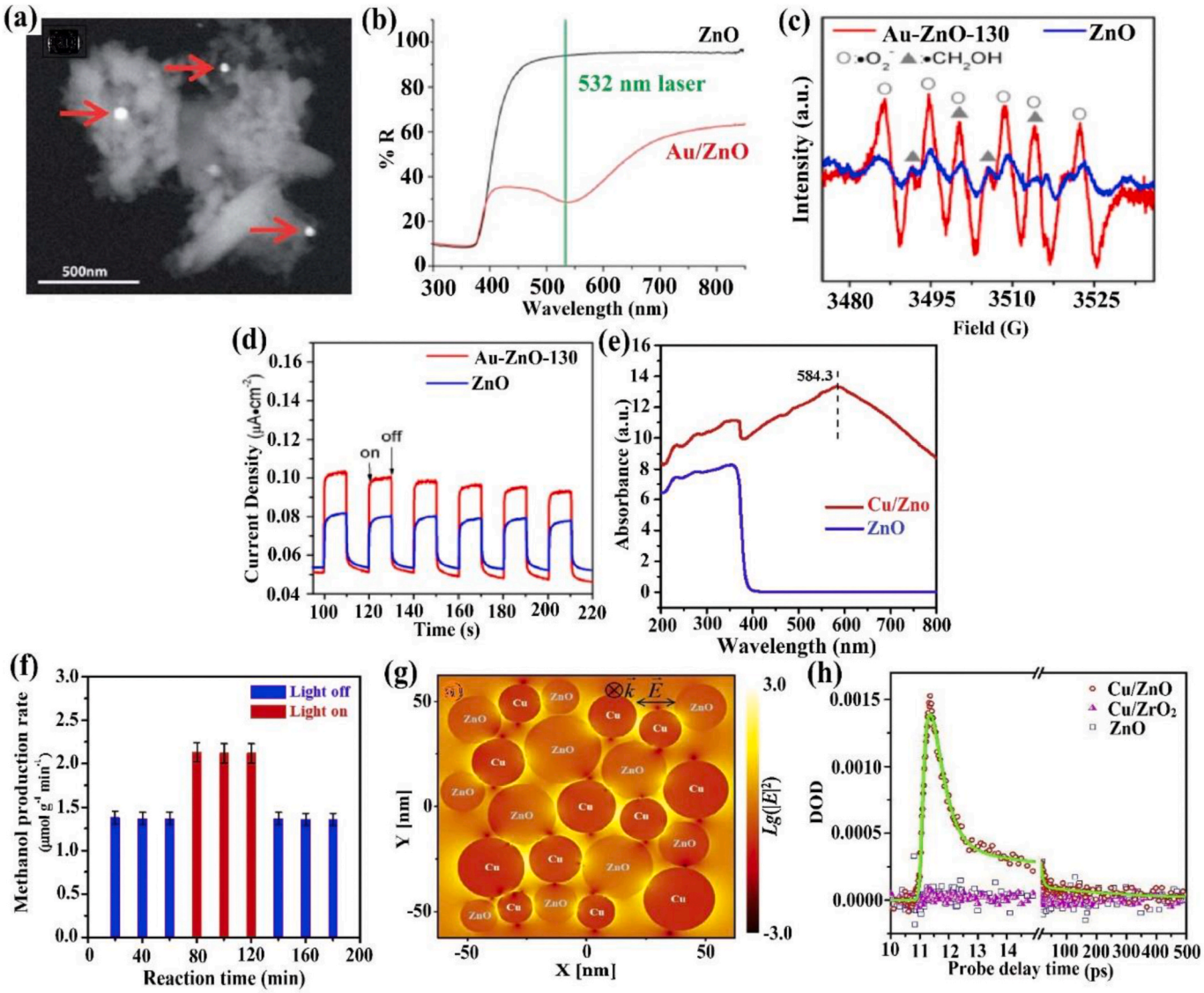

Fig. 15. (a) SEM image of Au–ZnO photocatalyst, **(b)** DRS analysis of Au–ZnO (red curve) and bare ZnO (black curve), **(c)** the electron paramagnetic resonance (EPR) spectrum of ZnO and Au–ZnO dispersed in 5,5-dimethyl-1-pyrolline-N-oxide solution, **(d)** photocurrent density-time arcs of bare ZnO and Au–ZnO samples, **(e)** UV–visible absorption spectrum of ZnO and Cu–ZnO photocatalyst, **(f)** CH_3OH generation rate with or with visible-light source at 220 °C, **(g)** the electromagnetic field distribution and **(h)** transient kinetic absorption investigations over Cu–ZnO photocatalyst under 580 nm light illumination. Reproduced with permission from refence (Wang et al., 2019c) under license number 4979251018580, 4979250899903, copyright 2013 Royal Society of Chemistry (2020) Wiley, and 2019 Elsevier. (For interpretation of the references to colour in this figure legend, the reader is referred to the Web version of this article.)

charge separation.

Shen and co-workers successfully synthesized the Au NR/ZnO photocatalyst via a feasible low-temperature solution method for solar-driven CO_2 photoreductions into CO (32.4 μmol g^{-1} h^{-1}) and CH_4 (17.12 μmol g^{-1} h^{-1}) (Shen et al., 2020b). Here, ZnO photocatalyst served the role of e^- acceptors by fetching hot e^- present in the core of Au NPs due to its two unique properties. Firstly, the high surface polarity induced the CO_2 activation by lowering the LUMO energy level and distorting the linear structure of CO_2. Secondly, excessive amounts of acidic protons and ·OH radicals were present at the ZnO surface, corresponding to CO_2 adsorption sites, which facilitated the solar-driven CO_2reduction-reaction. These free radicals were detected by electron paramagnetic resonance (EPR) analysis and O_2^-species yielded from CH_3OH and 5,5-dimethyl-1-pyrolline-N-oxide (DMPO) solutions. As shown in Fig. 15c, the characteristics peaks of DMPO-·CH_2OH and DMPO- O^{2-}solution was responsible for the generation of ·CH_2OH and O_2^- species, respectively. The strong peaks for Au NR/ZnO in comparison to bare ZnO indicated the improved photogenerated charge carriers under visible-light illumination (λ = 534 nm). Furthermore, the photocurrent-time (I-t) curves displayed increased photocurrent density for Au NR/ZnO than bare ZnO, thereby, revealed that coating Au core strengthened the light absorptivity to visible-region and photocatalytic performance (Fig. 15d).

Compared with the most studied Ag and Au NPs, the Cu NPs possessed intrinsic long-wavelength SPR mechanism but difficult to feasibly synthesize due to their sensitive nature towards oxidation. Recently, Wang and co-workers gave the first-time report on CH_3OH synthesis over Cu NPs/ZnO photocatalyst *via* CO_2 photoreduction under atmospheric pressure (Wang, Z.-j. et al., 2019). The Cu/ZnO photocatalyst was prepared by co-precipitation technique using 0.1 M Zn $(NO_3)_2.6H_2O$ and 0.05 M Cu $(NO_3)_2.3H_2O$ chemicals. Here, visible-light (absorption peak~ 584.3 nm) worked as an external incentive, increasing methanol production rate up to 2.13 μmol g^{-1} min^{-1} with decreased activation energy (49.4 kJ mol^{-1}) (Fig. 15e and f). The electromagnetic field was spatially dispersed over Cu/ZnO photocatalyst under 580 nm illumination, which induced photoexcitation of hot e^-

from Cu NPs surface to the ZnO through the interfacial region (Fig. 15g). Besides, transient absorption dynamic studies also confirmed the hot e^- migration route at Cu/ZnO interface as no transient peak was observed for Cu NPs, facilitating photoreduction reactions (Fig. 15h). Therefore, this work demonstrated the synergistic effect between Cu NPs and ZnO interface towards CH_3OH synthesis *via* CO_2 photoreduction.

4.4. Hetero-structuralization

The hetero-structuralization design is promising among variant strategies due to its advantages in separating photoinduced EHP and utilization of respective useful features of each component (Zhang, W. et al., 2020). The band alignment of constructed heterostructure must be equivalent to one another and follows the typical charge migration route, including Type-II, indirect Z-scheme, direct Z-scheme, and emerging Step-scheme, as shown in Fig. 16. The type-II configuration is one of the most typical heterostructures constructed by assembling two SC with staggered band alignment (Fig. 16a). In detail, under sufficient visible-light illumination, e^- transference takes place from the CB of SC-II to the CB of SC-I, while photogenerated h^+ in the VB of two SC follow a reverse stimulation. In this case, the photogenerated h^+ and e^- are accumulated on SC-I for an oxidation reaction and SC-II for reduction reaction, respectively, which reduced EHP recombination and enhanced carrier separation along with photoconversion efficiency of solar energy (Chen et al., 2020). Although type-II charge migration seems perfect due to its efficient charge separation from a closer view, it exhibits several inadequacies. Firstly, from a thermodynamic viewpoint, the promoted charge separation efficiency is at the expense of reduced redox ability, which is unfavourable for the CO_2 photoreduction reaction. Secondly, an electrostatic repulsive force from existing e^- in SC-II will hamper the continuous flow of e^- from SC-I. Hence, an imperious need is needed to develop a more efficient photocatalytic system along with superior redox abilities, EHP separation, and maximum light-harvesting capability. Fig. 16b represents the modified route of photoexcited EHP for the same constructed heterostructure, which is highly required due to its merits over type-II mode (Rodríguez-González et al., 2020). Typically, for an indirect Z-scheme photocatalyst system, including traditional Z-scheme and all-solid-state Z-scheme, two distinct SC are coupled through a suitable shuttle redox mediator. However, these redox mediators like Fe^{3+}/Fe^{2+} possessed back reactions while solid mediators like Ag, Au NPs displayed a light-shielding effect, high synthesis cost, and pH sensitivity, which decreased the photocatalytic activity efficiency. On the contrary, indirect Z-scheme charge carrier migration route, h^+ with high oxidative ability in the VB of SC-II and e^- with relatively strong reductive abilities in the CB of SC-I are preserved, whereas correspond e^-, and h^+ with inferior redox potential recombine (Fig. 16c) (Stelo et al., 2020).

S-scheme heterostructure formation is a new theoretical system concept, which was initially introduced in 2019 (Fu et al., 2019). In this case, the charge migration route is like "N" or "step" shape between two distinct n-type photocatalysts. During the charge kinetic phenomenon, the in-built internal electric field is a driven force among two photocatalyst, which induces spatial EHP separation. As Fig. 16d displayed, effective photoexcited e^- and h^+ can be used efficaciously to obtain reduction process, whereas useless e^- and h^+ would instantly recombine (Ge et al., 2019; Modic et al., 2019).

As for heterogenous photocatalysis, photocatalytic reactions occur at the surface of photocatalyst where preliminary adsorption of the contaminant is essential for a highly effectual process. For gas reactants/organic molecule-related reactions, it is of prodigious importance to comprehend the reactant adsorption on the photocatalyst surface as surface reactions plays a very critical role in the photocatalysis mechanisms. The CO_2 adsorption and its activation influence the successive CO_2 reduction reactions. Particularly for gaseous reactant reactions, the crucial step is to adsorb the gaseous molecule on the surface of photocatalyst, facilitating redox reactions with suppression of competing for

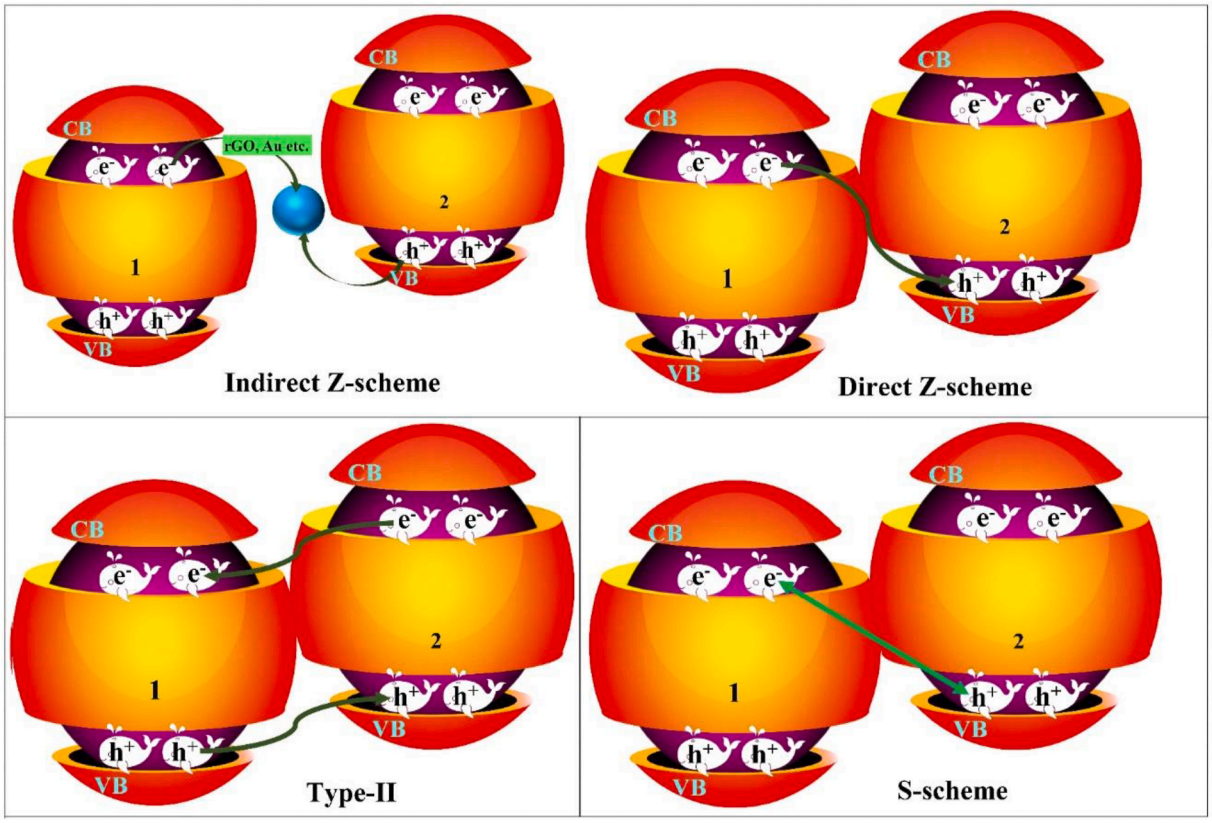

Fig. 16. Schematic illustration of the conduction band and valence band structures of different heterostructure types among the semiconductor photocatalyst.

one. For instance, a ternary Ag–Cu_2O/ZnO NR heterogeneous photocatalyst has been proved to exhibit maximum CO_2 adsorption capacity compared to pristine ZnO towards photoconversion of CO_2 into CO (Zhang et al., 2020). Here, the deposition of Cu_2O into the ZnO surface promoted the CO_2 adsorption capacity because of the bonding between the Cu site and the C atom of CO_2. Besides, the two desorption peaks at temperatures 427.6 and 274.1 °C, indicated the generation of robust adsorption active centres. Moreover, recently synthesized ZnO-based nanocomposites exhibited high enough specific surface area, such as C–ZnO/TiO_2@ZIF-8 (1309.5 m^2/g) (Wang, H.-T. et al., 2019), K-g-C_3N_4/ZnO NR (33.4 m^2/g) (Jin et al., 2020), Ag–ZnO/graphene oxide (120 cm^2/g) (Singh et al., 2013). Therefore, the ultra-high surface area of the photocatalyst has the most active sites for surface CO_2 adsorption, which promotes the CO_2 reduction process.

4.4.1. *Type-II based hetero-structuralization*

The coupling of two different SCs photocatalysts with staggering energy band structure, *i.e.,* type-II heterostructure, is the most favorable one, which provides spatial charge carrier separation, thus affording enhanced photocatalytic activity. Li and co-researcher successfully prepared a polydopamine loaded hollow ZnO/Co_3O_4 p-n heterostructure photocatalyst using pyrolyzing bimetallic Zn/Co-ZIFs towards CO_2 photoreduction in the presence of dimethylformamide (DMF)/H_2O mixture solution (Li et al., 2020). The hybrid photocatalyst provides 1.4 times increase in CO_2 reduction performance, exhibiting a CO yield of 537.5 μmol g^{-1} h^{-1} with 97.7% CO selectivity. Under UV–visible light illumination, photoexcitation of e^- and h^+ occurs at the ZnO/Co_3O_4 surface, but a discontinuity in the CB potentials of both SC brought difficulty in e^- transference, while h^+ migrated quickly to the corresponding VB. Thus, e^- remained in the CB of ZnO, acting as reductive photocatalyst and h^+ transport to the VB of Co_3O_4, giving efficient charge carrier separation. The CO_2 photoreduction proposed mechanism over ZnO/Co_3O_4 hybrid was depicted in the following eq. steps (Fig. 17a and b):

$$Co_3O_4\ /ZnO + h\nu \rightarrow Co_3O_4\ (e^-, h^+)\ /\ ZnO(e^-, h^+) \quad (4)$$

$$Co_3O_4\ (e^-, h^+)\ /\ ZnO(e^-, h^+) \rightarrow Co_3O_4\ (h^+)\ /\ ZnO(e^-) \quad (5)$$

$$ZnO(2e^-) + 2H^+ + Co_2 \rightarrow ZnO + H_2O + CO \quad (6)$$

$$Competiting\ reaction:\ 2H^+ + 2e^- \rightarrow H_2(g) \quad (7)$$

$$Co_3O_4\ (2h^+) + H_2O \rightarrow Co_3O_4\ + 1/2O_2 + 2H^+ \quad (8)$$

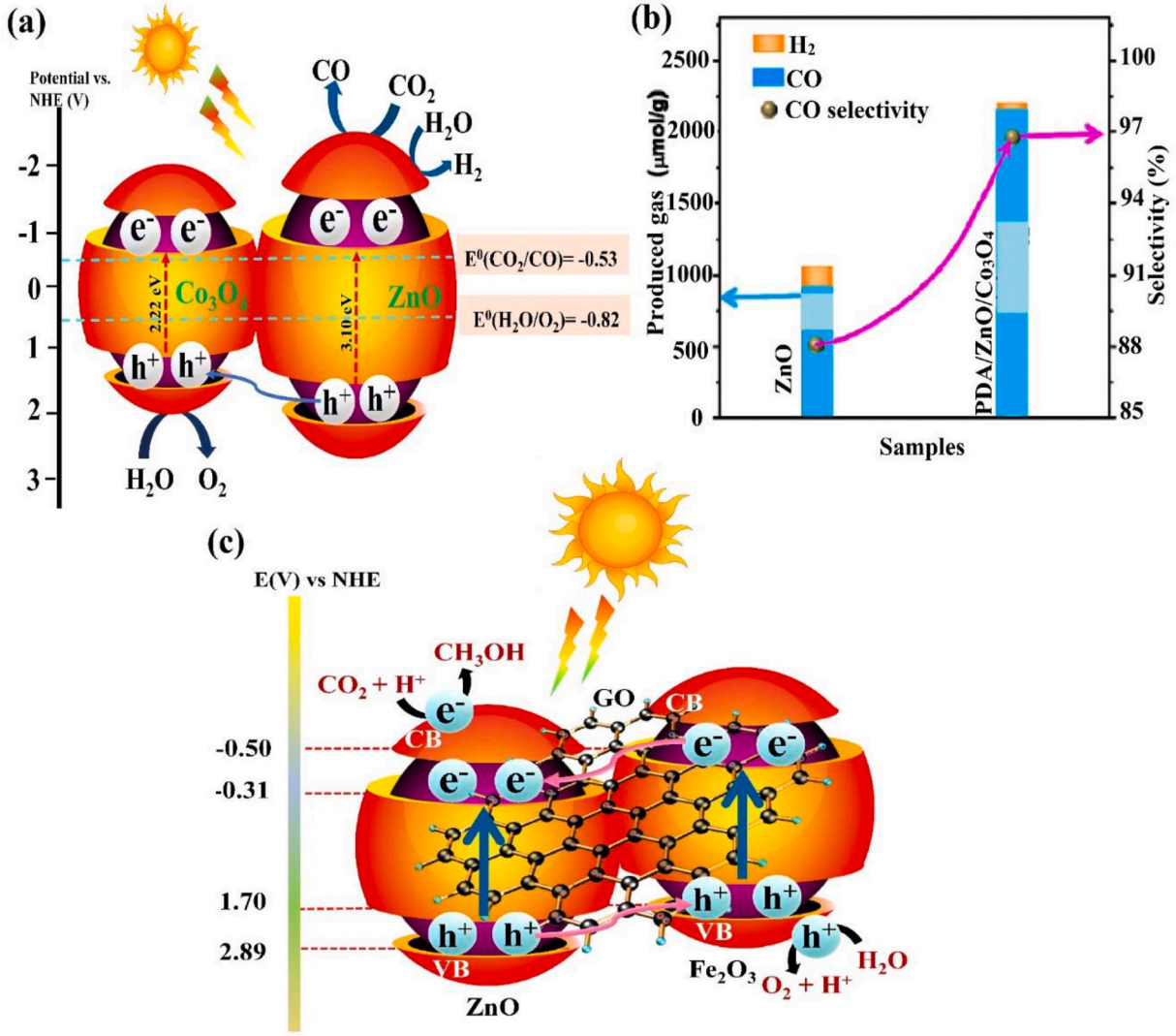

Fig. 17. (a) The proposed photocatalyst mechanism for CO_2 photoreduction over PDA/ZnO/Co_3O_4, **(b)** H_2 and CO production rate of ZnO and PDA (15 wt%)/ZnO/Co_3O_4 photocatalyst, and **(c)** schematic charge transfer pathway with CO_2 reduction mechanism for ZnO/Fe_2O_3/rGO photocatalyst. Reproduced with permission from Ref (Zhang et al., 2020b). under license number 4980140711057, copyright 2020 American Chemical Society and 2019 Elsevier.

Assembly of ZnO NR and α-Fe_2O_3 with reduced graphene oxide (ZnO-α-Fe_2O_3/rGO) heterostructure in a staggered band alignment enabled extended visible-light-driven photocatalytic CO_2 conversion into methanol with a yield of 1.8 μmol g^{-1} h^{-1} (Wang, X. et al., 2019). The possible mechanism for CO_2 conversion into methanol over ZnO-α-Fe_2O_3/rGO heterostructure has been depicted in (Fig. 17c). Photoexcited e^- from the 0.50 V CB of α-Fe_2O_3 (2.2 eV of narrow band energy) transported to the rGO layer and were further migrated to the 0.31 V CB of ZnO NR having 3.2 eV bandgap. Meanwhile, h^+ transportation occurs from 2.89 V VB of ZnO to the 1.70 V VB of α-Fe_2O_3. Therefore, the present band alignment prolonged the time-span of e-at the ZnO surface and enhanced the EHP separation efficiency, which increased the photocatalytic reduction reaction.

However, the type-II heterostructure exhibits some drawbacks of reduced redox ability of charge carriers due to the present transfer pathway, which induced the researchers to delve into a more effective photocatalytic system with superior redox ability, i.e., Z-scheme. The more detailed reports on modified ZnO based heterogeneous photocatalyst has been listed in Table 1 (Ali et al., 2018; Cai et al., 2018; Ehsan and He, 2015; Guo et al., 2020; Guo et al., 2016; Hanahan and Coussens, 2012; Iqbal et al., 2018a; Iqbal et al., 2018b; Jang et al., 2015; Karamian and Sharifnia, 2018; Li et al., 2013; Lingampalli et al., 2018; Liu, 2016; Shao et al., 2017; Taraka et al., 2019; Tiegel et al., 2015; Wang et al., 2016; Wu et al., 2018a; Xia et al., 2016).

Table 1
Summary of representative Type-II heterogeneous photocatalyst for CO_2 photoreduction.

Photocatalysts	Synthesis method/Precursors	Process parameter	Reaction conditions	Products (Max. yield)	Ref.
$BiFeO_3$–ZnO	Hydrothermal/Bi $(NO_3)_3{\cdot}5H_2O$, Fe $(NO_3)_3{\cdot}9H_2O$, Zinc acetate dihydrate	Distilled water	125 W high-pressure Hg arc lamp, λ = 485 nm, 2 mg photocatalyst, 30.0 mL KOH solution (8.0 M), 200 °C for 6h	CH_4 (21 μmol g^{-1} h^{-1}) with 1:1M ratio of $BiFeO_3$–ZnO	Karamian and Sharifnia (2018)
Co_3O_4–ZnO	Seed-mediated solvothermal/ Zinc acetate dihydrate, lilac powder, $CoCl_2{\cdot}6H_2O$	Deionised water	300 W Xe arc lamp, 0.1 g photocatalyst, 3 mL deionised water, 80 KPa pure CO_2 gas, 400 °C for 2h	CH_4 (0.99 μmol g^{-1} h^{-1})	Wang et al. (2016)
ZnO nanorod arrays/carbon fibres	In-situ growth process/Zn $(NO_3)_3{\cdot}6H_2O$, raw carbon fibres, HNO_3	Water/NaOH	12 mW cm^{-2}, UV lamp, λ = 254 nm, 1.0 g photocatalyst, 353K for 3 h, 40 mL ethanol NaOH solution,	CH_3OH (430.2 μmol g^{-1})	Liu (2016)
Cu_2O-Tipped ZnO nanorod	Photochemical deposition/ $CuSO_4$, Zn $(NO_3)_3{\cdot}6H_2O$	NaOH	120 mW cm^{-2}, 300 W Xe arc lamp, λ = 420 nm, 0.25 mol L^{-1} Na_2SO_3 and 1.0 mol L^{-1} NaOH aqueous solution, 1 g of photocatalyst, 28–30 kPa atm pressure, 90 min for 8 h, pH~ 6.8	CO (8.0 mol cm^{-2} h^{-1})	Iqbal et al. (2018b)
CuO–ZnO	Hydrothermal/Zn $(NO_3)_3{\cdot}6H_2O$, Cu $(CH_3COO)_2{\cdot}H_2O$, EDTA	Deionised water containing triethylamine (TEA)	85 W m^{-2}, 20 W white cold LED flood light, λ = 375 nm, dimethylamine/TEA/water (30/10/10 mL) aqueous solution, 100 mg of photocatalyst, pH~10	CH_3OH (3855.36 μmol g^{-1})	Taraka et al. (2019)
Au–ZnTe/ZnO nanowire array	Dissolution-recrystallization/ Zn $(CH_3COO)_2{\cdot}2H_2O$	Deionised water	100 mW cm^{-2}, 300 W Xe arc lamp, λ ≤ 550 nm, 0.5 M saturated potassium bicarbonate solution, pH~ 7.5, 300 °C for 2h	CO (115 mol cm^{-2} min^{-1})	Jang et al. (2015)
ZnO/ZnTe	Electrochemical deposition/Zn $(NO_3)_3{\cdot}6H_2O$, tellurium chloride, Zinc chloride	Water	300 W Xe lamp with cut-off filter, λ > 420 nm, 30 kPa atm pressure, 0.25 mol/L Na_2SO_3 and 1 mol/L NaOH, 15 °C for 8h	CH_4 (0.04 μmol cm^{-2} h^{-1})	Iqbal et al. (2018a)
ZnO/ZnTe	One-pot hydrothermal/ Na_2TeO_3, Zn $(NO_3)_3{\cdot}6H_2O$,	NaOH solution	300 W Xe lamp with cut-off filter, λ ≥ 420 nm, 20 mg of photocatalyst, 25 kPa atm pressure, 0.15 M aqueous solution of NaOH, 180 °C for 8h	CH_4 (221.05 μmol g^{-1})	Ehsan and He (2015)
ZnO/reduced graphene oxide (rGO)	One-step hydrothermal/ $K_2S_2O_8$, flake graphite, Zinc chloride	Distilled water	500 W Xe lamp, λ = 520 nm, 100 mg of photocatalyst, 100 mL of 0.0025 M $NaHCO_3$ aqueous solution,	CH_3OH (45.75 μmol g^{-1})	Li et al. (2013)
ZnO/rGO	One-step hydrothermal/ $K_2S_2O_8$, graphene oxide, zinc nitrate	Deionised Water	300 W Xe lamp, λ ≥ 420 nm, 100 mg of photocatalyst, 50 mL 1.0 M NaOH solution, pH~ 8, 3h reaction time	CH_3OH (263.17 μmol g^{-1})	(Zhang et al., 2015)
ZnO/Cu–Zn–Al-layered doubled hydroxide	Deposition-precipitation/Zn $(NO_3)_2{\cdot}6H_2O$, polyvinyl pyrrolidone,	Water	UV–visible light, λ > 370 nm, 5 M NaOH aqueous solution, 2.0 g solution of Cu^{2+}, Zn^{2+} and Al^{3+} (0.05 mol/L each concentration), 9.0 mmol of Na_2CO_3 and 3.6 mmol of NaOH in 60 mL aqueous solution	CH_4 (58 μmol g^{-1})	Guo et al. (2016)
ZnO/$Ag_{1-x}Cu_xCdS$	Hydrothermal/Zinc acetate dihydrate, $CuSO_4{\cdot}5H_2O$, $AgNO_3$	2-propanol and water	450 W Xe lamp with a UV cut-off filter, λ > 395 nm, 20 mg of photocatalyst, 0.4 M $NaHCO_3$, pH~ 12, 2h reaction time	CO (327.4 μmol g^{-1} h^{-1})	Lingampalli et al. (2018)
ZnO quantum dot/ KNb_3O_8	Two-step hydrothermal/ Nb_2O_5, $ZnCl_2$	Isopropanol	250 W high-pressure Hg arc lamp, λ = 365 nm, 20 mg of photocatalyst, pH~ 6, 10h reaction time	CH_3OH (1539.77 μmol g^{-1} h^{-1})	Shao et al. (2017)
Ti/ZnO/Fe_2O_3	Calcination/titanium tetrachloride, diethyl ether, Zn $(NO_3)_3{\cdot}6H_2O$, Fe $(NO_3)_3{\cdot}9H_2O$	Deionised water	300 W Xe lamp, λ ≥ 400 nm, pH~ 8, 800 °C for 3h, 150 mL of ethanolic solution, 120 mL containing 30.0 g NaOH aqueous solution	CH_3OH (0.773 mmol cm^{-2} h^{-1})	Wu et al. (2018a)
TiO_2/ZnO	Sol-gel and hydrolysis/Zn $(NO_3)_3{\cdot}6H_2O$, tetra-n-butyl,	Deionised Water	300 W Xe lamp with 200–1700 nm cut-off filter, 100 mg of photocatalyst, pH~ 25, 3 h reaction time	CH_4 (2.56 μmol g^{-1} h^{-1})	Xia et al. (2016)
ZnO nanorod array/ graphene	Dipolar binary liquid/C_6H_6, $NH_3{\cdot}H_20$, graphene	Water	12 mW cm^{-2}, 300 W Xe arc lamp, λ = 254 nm 0.1 g of photocatalyst, 3 h reaction time	CH_3OH (375 μmol g^{-1})	Liu and Jin (2017)
Core@shell-ZnO/ ZnSe	Dissolution-recrystallization/ Zinc acetate dehydrate, Zn $(NO_3)_3{\cdot}6H_2O$, $NaBH_4$	$NaHCO_3$	100 mW cm^{-2},150 W Xe lamp with AM 1.5G filter, pH~ 7, 12.6 mM and 88.2 mM $NaBH_4$ aqueous solution, 90 °C for 20 h	CO (1.6 μmol cm^{-2} h^{-1})	Cai et al. (2018)
Bi_2O_3-graphene-ZnO	Ultrasonication/Bi $(NO_3)_3{\cdot}5H_2O$, ethanol, nitric acid, Zn $(NO_3)_3{\cdot}6H_2O$	Distilled water	500 W Solar Edge-700 metal halide lamp, 150 mg of photocatalyst, 50 mL of aqueous solution of sodium bicarbonate, 12 h reaction time	CH_3OH (7.250 μmol g^{-1} h^{-1})	Ali et al. (2018)
ZnO nanosheet/g-C_3N_4	Solvothermal/Zinc acetate, melamine, thiourea	Deionised Water	300 W Xe lamp with a UV cut-off filter, λ > 420 nm, 50 mL of ethylenediamine as solvent, 200 °C for 4 h	CH_4 (30.5 μmol g^{-1} h^{-1}) and CO (16.8 μmol g^{-1} h^{-1})	Guo et al. (2020)

4.4.2. Indirect or direct Z-scheme based hetero-structuralization

To mimic natural photosynthesis, the traditional Z-scheme photocatalytic system is an effective strategy for converting CO2 with water into solar fuels and simultaneously preserving strong redox potentials (Xue et al., 2020). The Z-scheme types depend on the need for an e^- mediator to accomplish the Z-scheme charge transfer route, which is further classified as direct or indirect. Table 2 presents the recent work on Z-scheme-based photocatalysts for CO_2 reduction (Makino and Shimizu, 2018; Nie et al., 2018a; Nie et al., 2018b; Shen, D. et al., 2020; Vickers, 2017; Zubair et al., 2017).

Recently, Li and his peer research group reported Au@ZnO/g-C_3N_4 (A-ZnCN) hybrid photocatalyst prepared using Au as charge transfer bridge through an impregnation-calcination method (Li et al., 2021). SEM results confirmed the micro-needle (MN) morphology and Au NPs loading on the ZnO surface. Also, high-resolution-TEM (HRTEM) analysis revealed the presence of a crystal plane (0.23 nm) corresponding to the crystal plane (Meng et al.) of Au NPs (Fig. 18a). The proposed mechanism of A-ZnCN hybrid photocatalyst under visible-light illumination ($\lambda = 560$ nm) was illustrated (Fig. 18b). A g-C_3N_4 being n-type SC possessed higher −1.6 V CB than the ZnO MN CB, *i.e.,* −0.6 V, and continuous e^- flow takes place till the time fermi level of both SC equilibrated. This e^- migration process induced the in-built internal electric field among the two SCs forming band-bending at ZnO MN surface while the band curved upwards for g-C_3N_4, which facilitated a number of e^- and h^+ at the hybrid surface. The finite difference time domain (FTDT) approach was employed to confirm the built-in internal electric field of the A3wt%-ZnCN hybrid. FTDT imitation determined the thickness of ZnO MN and g-C_3N_4 as 10 and 6 nm, respectively, along with the size of Au NPs as 40 nm (Fig. 18c). Fig. 18d and e displayed the electromagnetic field increment of A3wt%-ZnCN under light illumination of $\lambda = 380$ nm and $\lambda = 550$ nm due to the SPR effect Au NPs which increased the EHP separation efficiency. Thus, A3wt%-ZnCN exhibited the maximum CO_2 conversion into CO, *i.e.,* 689.7 μmol m^{-2}, which was about 2 or 4.5 times greater than Au–ZnO (355.5 μmol m^{-2}) or bare ZnO (155.5 μmol m^{-2}).

Apart from Au NPs, rGO is also a substitute e^- mediator to construct Z-scheme heterostructure. For instance, the metal-organic framework based UIO-66-NH_2/rGO/oxygen deficient-ZnO (UIO-66-NH_2/rGO/O–ZnO) Z-scheme photocatalyst was fabricated by the solvothermal method (Meng et al., 2019). Electron spin resonance (ESR) spectra indicated the presence of oxygen-vacancy in UIO-66-NH_2/rGO/O–ZnO during solvothermal synthesis (Fig. 19a). The weak peak of PL spectra obtained at $\lambda = 465$ nm for UIO-66-NH_2/rGO/O–ZnO hybrid revealed the sufficient interfacial EHP separation between O–ZnO and UIO-66-NH_2 (Fig. 19b). The photocatalytic mechanism for Z-scheme structure occurred when photoexcited e^- at the CB of O–ZnO transferred through rGO layer to the VB of UIO-66-NH_2, where e^- got accumulated and which further reduced CO_2 into 6.41 μmol g^{-1} h^{-1} HCOOH and 34.83 μmol g^{-1} h^{-1} CH_3OH (Fig. 19c and d). Thus, the Z-scheme mechanism route not only minimized the EHP recombination rate but also maintained strong reductive and oxidative abilities.

Zhang and co-workers reported the Ag@Cu_2O/ZnO ternary heterostructure formed when Cu_2O and Ag NPs were incorporated into ZnO NR through a solvothermal and chemical reduction approach (Zhangetal., 2020). The maximum yield of CO production rate was obtained for Ag (0.6 wt%)-Cu_2O(0.4 wt%)/ZnO (13.45 μmol g^{-1}) with 0.0547% quantum efficiency than binary Cu_2O/ZnO heterostructure (8.14 μmol g^{-1}) under 4 h of light illumination ($\lambda = 400$ nm). The Ag(0.6 wt%)-Cu_2O (0.4 wt%)/ZnO photocatalyst possessed the most excellent transient photocurrent density due to the synergistic effect of Cu_2O and Ag in which Ag NPs served as e^- trapping agent (Fig. 19e). Further, the EIS Nyquist plot of Ag(0.6 wt%)-Cu_2O(0.4 wt%)/ZnO displayed the smaller semicircle arc than bare ZnO and Cu_2O/ZnO, indicating the lowest charge migration resistance and enhanced separation efficacy at interfacial contact (Fig. 19f). Moreover, under UV–visible light irradiation, fluorescence spectrum peak at 428 nm increased with the illumination time, indicating a gradually increased rate of ·OH concentration at the interface. In a photocatalytic Z-scheme mechanism route, selective photoexcitation of e^- occurred from the −0.57 V CB of ZnO to the 0.91 V VB of Cu_2O under visible-light illumination ($\lambda \geq 432$ nm). Meanwhile, photoinduced h^+ were aggregated at the 2.59 V VB of ZnO illustrated through the following eq. steps:

$$H_2O + h^+ \rightarrow \bullet OH + H^+ \quad (9)$$

$$\bullet OH + \bullet OH \rightarrow H_2O + 1/2O_2$$

Here, e^- were trapped by Ag NPs with low fermi energy from the −1.22 V CB of Cu_2O, which suppressed the EHP recombination rate and maintained heterostructure stability.

4.4.3. S-scheme based hetero-structuralization

Categories by band-energy structures, semiconducting materials are divided as oxidative photocatalyst (OP) and reductive photocatalyst (RP), where RP exhibits higher CB mainly employed in the formation of solar fuels. On the contrary, OP is mostly applied in the environmental degradation processes due to their potential photogenerated holes, which participated in the degradation reactions. In RP, photoexcited electrons participated in reduction reactions whereas, photogenerated holes are fruitless and need to be amended by sacrificial agents.

A novel step-scheme (S-scheme) heterostructure has been proposed, which comprised OP and RP with staggered band alignment attains sufficient EHP separation (Jamwal et al., 2020). In a conventional

Table 2
Summary of representative Z-scheme based photocatalyst for CO_2 photoreduction.

Photocatalyst	Electron transfer	Synthesis method [Precursor]	Process parameter	Illumination [Performance]	Ref.
Polydopamine/ZnO hierarchical microspheres	Direct Z-scheme	Self-assembly (benzene, hydroxyl, Zn $(NO_3)_3{\cdot}6H_2O$)	Na_2SO_4	UV lamp, $\lambda = 365$ nm, CH_3OH: 0.9 μmol g^{-1} h^{-1} and CH_4: 0.25 μmol g^{-1} h^{-1}	Nie et al. (2018a)
g-C_3N_4/ZnO	Direct Z-scheme	One-step facile calcination (550 °C, 2h), (urea, zinc nitrate hexahydrate)	$NaHCO_3$ and HCl	300 W Xe arc lamp, $\lambda = 365$ nm, CH_3OH: 0.6 μmol g^{-1} h^{-1}	Yu et al. (2015)
g-C_3N_4/ZnO microsphere	Direct Z-scheme	Hydrothermal-calcination and electrostatic self-assembly (120 °C, 6h and 550 °C, 2h), (Zn $(NO_3)_3{\cdot}6H_2O$, $CO(NH_2)_2$, $Na_3C_6H_5O_7{\cdot}2H_2O$)	H_2SO_4 and $NaHCO_3$	80 mW cm^{-2},4W LED, $\lambda = 365$ nm, CH_3OH: 1.32 μmol g^{-1} h^{-1}	Nie et al. (2018b)
ZnO/g-C_3N_4	Direct Z-scheme	One-step calcination (urea, zinc acetate, hexamethylenetetramine)	Deionised water	300 W Xe arc lamp, $\lambda \geq 420$ nm, CH_4 and CO: 50 μmol g^{-1} h^{-1} and 70 μmol g^{-1} h^{-1}	Shen et al. (2020a)
Cu_2ZnSnS_4/ZnO	Direct Z-scheme	Calcination and hydrothermal (400 °C, 2h and 180 °C, 18h) (copper (II) nitrate trihydrate, zinc chloride, tin (II) chloride, sodium sulphide)	Deionised water	Solar light with AM 1.5 cut off-filter, $\lambda =$ 532 nm, CH_4: 138.94 ppm g^{-1} h^{-1}	Zubair et al. (2017)
ZnO/g-C_3N_4/$ZnWO_4$	Double Z-scheme	Stepwise-calcination (140 °C, 6h), ($(NH_4)_6W_7O_{24}6H_2O$, Zn $(NO_3)_3{\cdot}6H_2O$, urea)	Deionised water	CO:1.12 μmol g^{-1} h^{-1}, CH_4:6.24 μmol g^{-1} h^{-1}, CH_3OH: 3.85 μmol g^{-1} h^{-1}, CH_3CH_2OH 1.98 μmol g^{-1} h^{-1}	[116]

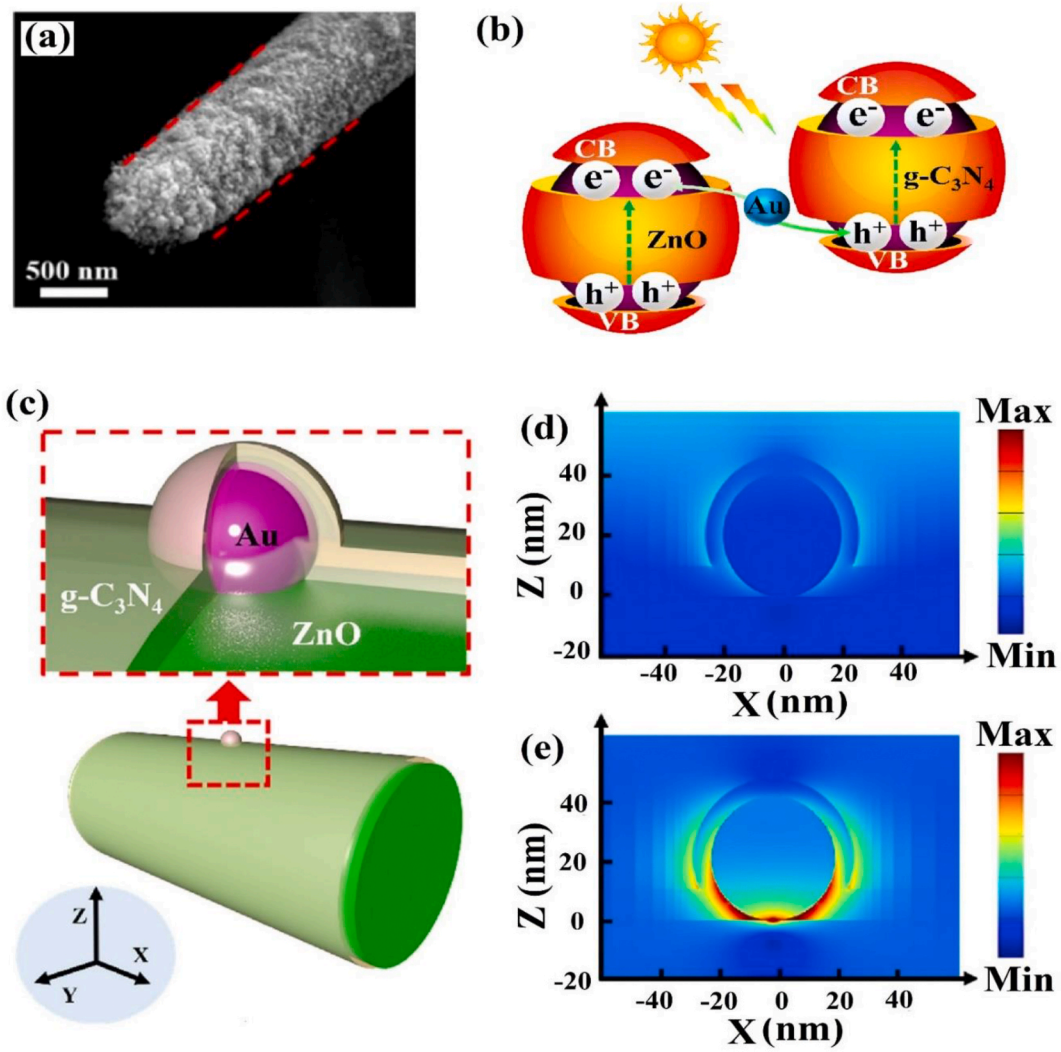

Fig. 18. (a) High-resolution SEM image of ZnO/Au/g-C_3N_4 prepared at 300 °C calcination temperature, **(b)** localized surface plasmonic resonance improved ZnO/Au/g-C_3N_4 Z-scheme heterostructure, **(c)** finite difference-time domain (FTDT) method simulation test result of ZnO/Au/g-C_3N_4 heterostructure under light excitation of wavelength **(d)** 380 nm, and **(e)** 550 nm. Reproduced with permission from Ref (Meng et al.). under license number 4980150194315, copyright 2020 Elsevier.

Type-II heterostructure, photoexcited h^+ and e^- are accrued on the VB of RP and CB of OP, respectively, revealing weak redox ability. S-scheme heterostructures comprising of two SC can preserve light-induced charge pairs with strong redox ability evidently on two SC, fulfilling the criteria of CO_2 photoreduction reaction. In an S-scheme heterostructure, an in-built IEF exists typically at the interfacial contact, which induces a continuous flow of e^- from CB of one SC to the VB of other SC, displaying an S-scheme transfer route. Here, the useful e^- and h^+ with strong redox capability are kept, while that useless e^- and h^+ with weak redox ability are recombined and removed. In this scheme, the charge carrier migration route has been explained as follows:

i. As shown in Fig. 20a, OP has a smaller CB and VB position and higher work function relative to RP. After the interfacial contact between two SCs, e^- at the RP surface diffuse to the OP, generating an e^- accumulation layer and e^- depletion layer near the OP and RP interface, respectively (Fig. 20b). An IEF is formed by positively charging RP to the negatively charged OP, facilitating the charge stimulation pathway from OP to the RP (Fig. 20c).
ii. During RP and OP contact, their Fermi level should equilibrate, resulting in downward and upward band bending in the fermi energy of the corresponding RP and OP, respectively. The downward band shift impulses the photogenerated h^+ at the VB of RP and e^- at the CB of OP interface to be recombined due to Coulombic attraction among e^- and h^+.
iii. The factors mentioned above, like Coulombic force, band bending, and IEF are the driving forces responsible for the recombination of h^+ and e^- present at the VB of RP and CB of OP, respectively. The remaining useful photoexcited e^- at the CB of RP and h^+ at the VB of OP further participated in the photocatalytic activity (He et al., 2020; Mu et al., 2020).

Recently, Cerrato and his peer group synthesized ZnO/g-C_3N_4 mixture of 50:50 M ratios of one-step thermal annealing technique at 823 K using Zn $(NO_3)_3{\cdot}6H_2O$ and melamine as a precursor (Cerrato and Paganini, 2020). From TEM results, the presence of ZnO NPs wrapped by the multilayer assembling structure of g-C_3N_4 was observed, indicating the interface region's formation (Fig. 21a). The EPR spectra of 50:50 mixed ZnO/g-C_3N_4 photocatalyst depicted improved photoactivity of ZnO and the successful interfacial region. During UV illumination, the intense peak of the signal was observed, while the minimum intensity of the peak was detected under visible-light irradiation ($\lambda = 455$ nm). The Lorentzian peak at $g = 2.0042$ was produced due to the existing e^- in the g-C_3N_4 (violet line), which was incorporated on the broader $g = 2.005$

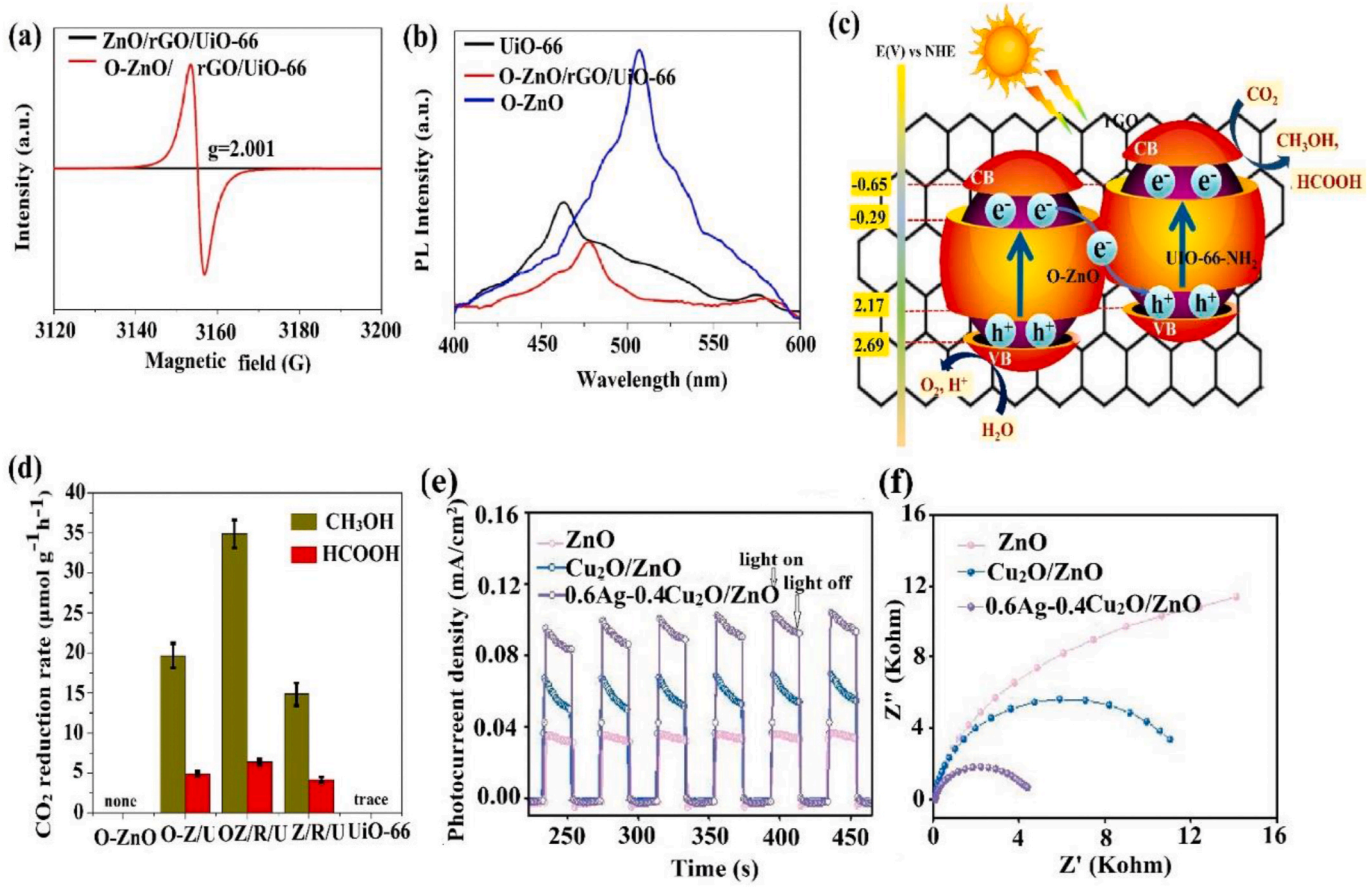

Fig. 19. (a) Electron spin resonance (ESR) analysis of ZnO/rGO/UiO-66 and O–ZnO/rGO/UiO-66, **(b)** PL spectrum of UiO-66-NH_2, O–ZnO, and O–ZnO/rGO/UiO-66-NH_2, **(c)** photocatalytic Z-scheme mechanism of O–ZnO/rGO/UiO-66-NH_2, (d) HCOOH and CH_3OH production rate for different samples, **(e)** Transient photocurrent absorption results and **(f)** electron impedance spectroscopy (EIS) Nyquist plots for ZnO, Cu_2O/ZnO, 0.6Ag-0.4Cu_2O/ZnO samples. Reproduced with permission from Ref. Meng et al. (2019) (Zhang et al., 2020a); under license number 4980160145646, copyright 2019 American Chemical Society, and 2019 Elsevier.

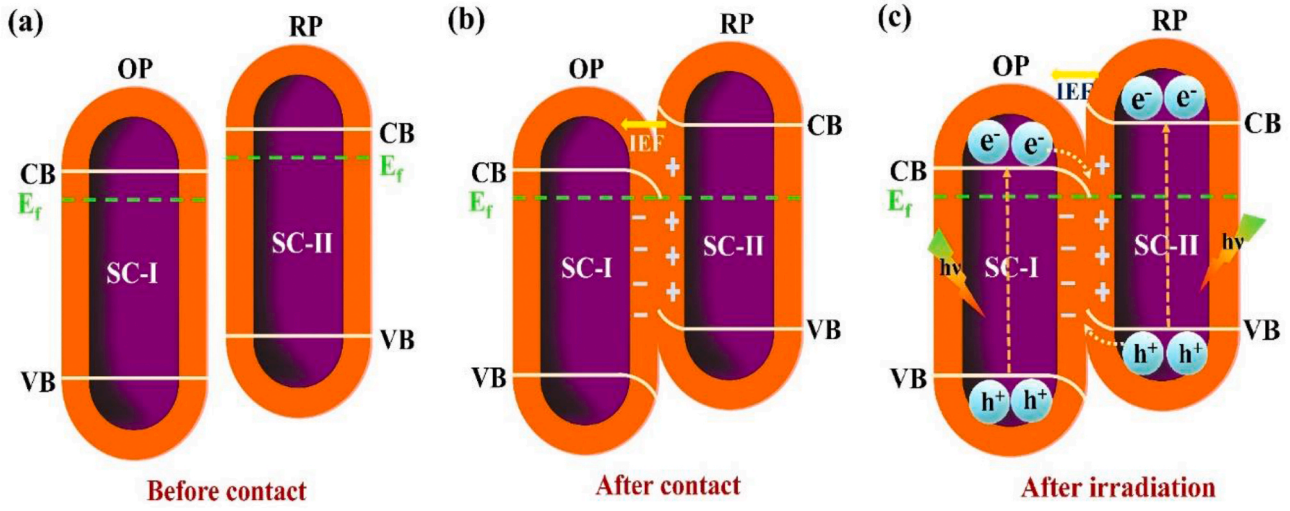

Fig. 20. Diagrammatic drawing of heterostructure with staggered band alignment; **(a)** before contact, **(b)** after contact, and **(c)** S-scheme charge transfer mechanism under light illumination.

module of the O^- site. However, in the S-scheme transfer pathway mechanism, the existing IEF at the interface facilitated the selective eradication of e^- in the lower 0.02 V CB of ZnO with the h^+ in the higher 1.57 V VB of g-C_3N_4. This described pathway ensured the maintained strong redox capability of photogenerated h^+ at ZnO VB (3.0 V) and e^- at g-C_3N_4 CB (−1.12 V) as displayed in (Fig. 21b) for further photocatalytic reactions.

In another work, a hierarchical Z-scheme photocatalyst ($ZnMn_2O_4$/ZnO) was fabricated by electrospinning and calcination methods with in-situ incorporation of ZnO (Deng et al., 2021). The resulting

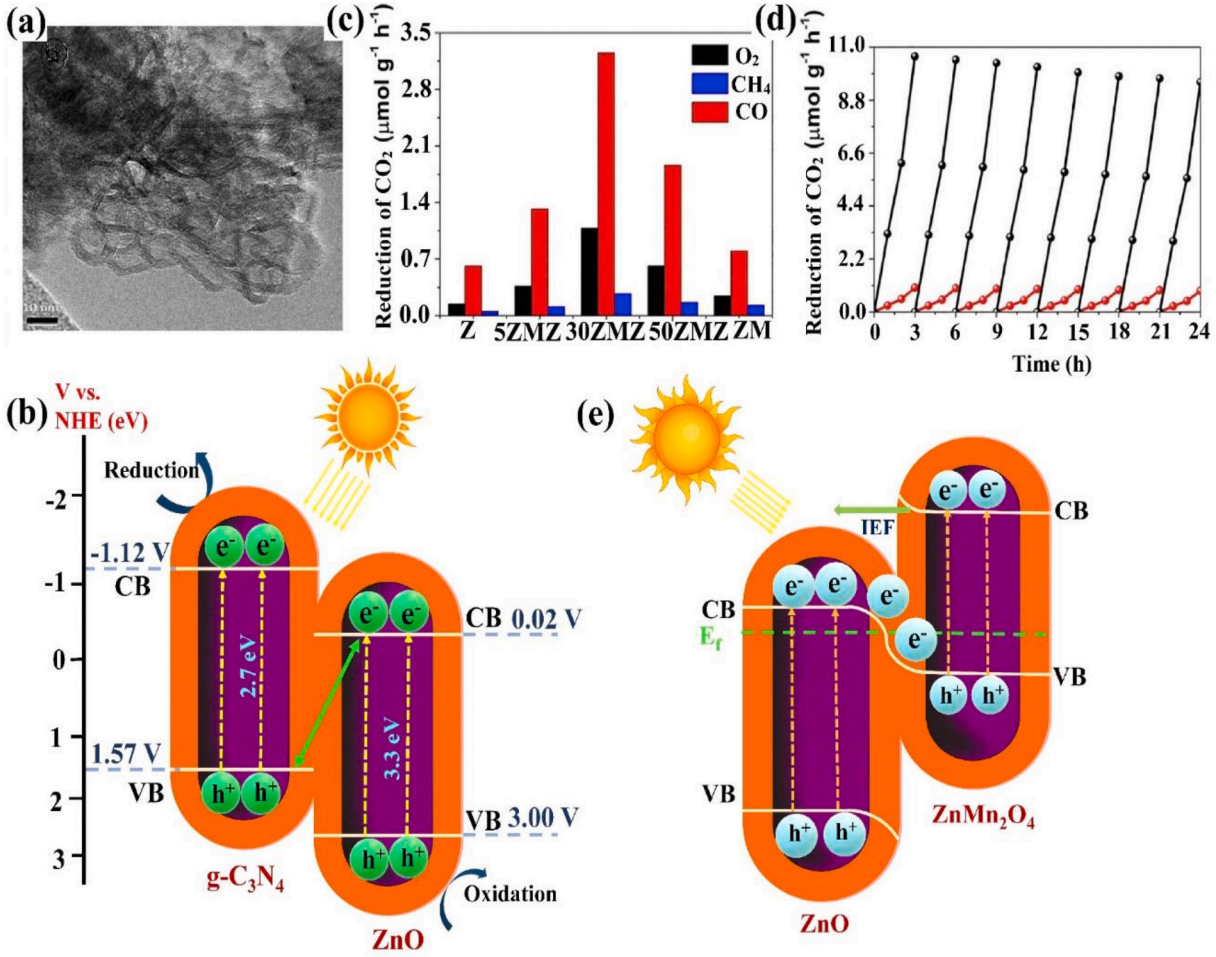

Fig. 21. Transmission electron microscopy (TEM) image of ZnO-g-C_3N_4, **(b)** schematic illustration of ZnO-g-C_3N_4 direct or S-scheme heterostructure based mechanism, **(c)** CO and CH_4 production rate for different samples, and **(d)** stability and recyclability test for 30ZMZ photocatalyst. Reproduced with permission from Ref (Cerrato and Paganini, 2020; Deng et al., 2021). under license number 4980251341379, copyright 2020 Royal Society of Chemistry, and 2020 Elsevier.

$ZnMn_2O_4$/ZnO (ZMZ) enabled effective photocatalytic CO_2 conversion into 3.2 μmol g^{-1} h^{-1} CO and 0.3 μmol g^{-1} h^{-1} CH_4 with stability up to 24 consecutive cycles (Fig. 21c and d). Photoexcitation of e^- takes place from $ZnMn_2O_4$ with a smaller work function of 4.55 eV to the ZnO (4.63 eV) until their fermi energy equilibrate. Thus, the $ZnMn_2O_4$ surface exhibited positive h^+, while e^- was accumulated at the ZnO interface, forming an e^- rich layer. Meanwhile, the band potential of ZnO was bent downwards, and simultaneously $ZnMn_2O_4$ band potential shifted upward due to loss of e^-. Besides, the driving forces inhibited the e^- flow from the $ZnMn_2O_4$ CB to the ZnO CB, forming an s-type route that endowed the heterostructure with strong reductive and oxidative abilities (Fig. 21e).

5. Challenges and future perspectives

The future of CO_2 mitigation depends on the photocatalytic CO_2 conversion into value-adding chemicals and fuels through photocatalysis. This review provides the recent research and advancements of modified ZnO photocatalyst for the photocatalytic CO_2 conversion to optimize the drawbacks of bare ZnO and significantly improve its photoactivity visible-light illumination. By employing specific modification strategies like doping, plasmonic metal loading, surface vacancy engineering, and hetero-structuralization, remarkable achievements have modified ZnO for CO_2 mitigation. To date, despite the considerable advancement in this field, challenges remain and hamper the practical implementation of the ZnO photocatalyst.

i. ZnO is more environment friendly, reusable, and stable than other photocatalysts but less photoactive due to its wide bandgap. Therefore, employing suitable modifications like doping and decoration with plasmonic metals to tune its large bandgap could be an attractive approach to extend the light absorption in the visible region.
ii. Although significant advances have been made in transforming CO_2 into C_1 products (like CO and CH_4) using modified ZnO photocatalyst, the yield of C_2 and C_3 hydrocarbon with high economic values, and large energy density is still minimal. Extensive research should be devoted to designing a photocatalyst with more active centres would be a key to understand the synergistic cascade reactions.
iii. The CO_2 selectivity and photoactivity are mainly determined by the loaded plasmonic metal (such as Ag, Au), or in detail, the interaction between surface cocatalyst and CO_2 molecule. However, the kind of interaction between CO_2 molecule and metal cocatalyst during the photoreduction process is unexplainable. These plasmonic metals, due to cost-ineffectiveness, are less explored on a commercial scale. A suitable cocatalyst should be chosen in order to understand this interaction mechanism in a more precise way. Future experimentation will require more advanced in-situ characterization techniques, more accurate DFT imitation, etc.
iv. The bottleneck of CO_2 photoreduction is the competing H_2 production reactions, which limit CO_2 selectivity towards a

particular product. Temporarily, the primary reductive product from CO_2 photoreduction is a mono-carbon product, whereas multi-carbon products (energy-rich) are highly followed. In such a case, the localized electronic structure of active sites should further engineer through surface vacancies and loaded metal nanoparticles to attain artificial photosynthesis.

v. Sometimes mixed photo-redox products may occur from the destruction of crystalline structure ZnO due to optical instability. To confirm whether the resultant product is derived from the CO2 molecule rather than carbon impurities, blank and isotopic labelling experiments are highly recommended by taking CO_2 and H_2O as reactants.

vi. Although there are many reports on ZnO-based Z-scheme photocatalyst, it is still in its infancy, especially in CO_2 photoreduction with some uncertain reductive product challenges, vague charge transport route, and inaccurate amount evaluation of the generated products. Further research should be devoted to advanced experiments and computational methods to afford an in-depth understanding of the charge transport pathway and reaction mechanism.

vii. Despite significant advancements in heterogenous photocatalysis, reports on S-scheme-based hetero-structuralization are still inadequate to deeply understand the charge-transport rules and roles of surface cocatalyst at the S-scheme interface. To this end, the combination of theoretical simulation and ex-situ and in-situ techniques can afford atomic and molecular-level insight into S-scheme heterostructure. Also, more research work should focus mainly on photocatalytic CO_2 reduction and other applications.

6. Conclusions

Photocatalytic conversion of green-house gas CO_2 into solar fuels through sunlight harvesting appears to be a key approach to alleviate global environmental issues and energy crises. The capability to transform an immensely stable CO_2 molecule into hydrocarbons is the leading research focus, utilizing suitable photocatalyst, reasonable reaction kinetics, and accessibility of light source. This review has emphasized the latest advances on modified ZnO-based photocatalyst for CO_2 reduction. A detailed discussion on CO_2 adsorption, activation, and reduction in the photocatalysis mechanism is given. Further, existing strategies have been presented to optimize the limitations of bare ZnO, such as small surface area, wide bandgap, low solar energy harvesting, deficient photo, and chemical stability. To achieve best photocatalytic activity, the strategies mainly focus on the free-carrier mobility and separation rate, maximum optical absorption, and the matched energy band configuration. The strategies such as coupling with surface plasmonic effect, metal and non-metal doping could significantly reduce the wide bandgap, giving improved light-harvesting capabilities. Moreover, strategies like oxygen vacancy creation, Z-schemes, and new emerging S-scheme based heterostructures with an in-depth mechanism are also delineated. Despite explosive progress and advances in this field, continuous research on improving modified ZnO photocatalyst performance is needed to attain substantial reactants conversions and product yield to implement at a wider-scale for solar fuel production.

Credit author statement

Shilpa Patial, Conceptualization, Methodology, Investigation, Writing – original draft. Rohit Kumar, Conceptualization, Methodology. Pankaj Raizada, Supervision, Conceptualization, Methodology, Investigation, Writing – original draft, Reviewing and Editing. Pardeep Singh, Conceptualization, Methodology, Investigation, Writing – original draft. Quyet Van Le, Conceptualization, Methodology. Eric Lichtfouse, Conceptualization, Methodology. Dang Le Tri Nguyen, Conceptualization, Methodology. Van-Huy Nguyen, Conceptualization, Methodology, Investigation, Reviewing and Editing.

Declaration of competing interest

The authors declare that they have no known competing financial interests or personal relationships that could have appeared to influence the work reported in this paper.

Acknowledgment

The corresponding author, Dr. Pankaj Raizada is thankful to H.P. Council for Science, Technology & Environment (HIMCOSTE) for financial support through HIMCOSTE research project no. (R&D)/2019-20-2.5(4).

References

Albero, J., Peng, Y., García, H., 2020. Photocatalytic CO2 reduction to C2+ products. ACS Catal. 10 (10), 5734–5749.
Ali, A., Biswas, M.R.U.D., Oh, W.-C., 2018. Novel and simple process for the photocatalytic reduction of CO 2 with ternary Bi 2 O 3–graphene–ZnO nanocomposite. J. Mater. Sci. Mater. Electron. 29 (12), 10222–10233.
Basumallick, S., 2020. Electro-reduction of CO 2 onto ZnO–Cu nano composite catalyst. Appl. Nanosci. 10 (1), 159–163.
Bo, Y., Gao, C., Xiong, Y., 2020. Recent advances in engineering active sites for photocatalytic CO 2 reduction. Nanoscale 12 (23), 12196–12209.
Cai, C., Xu, Y.-F., Chen, H.-Y., Wang, X.-D., Kuang, D.-B., 2018. Porous ZnO@ ZnSe nanosheet array for photoelectrochemical reduction of CO2. Electrochim. Acta 274, 298–305.
Cerrato, E., Paganini, M.C., 2020. Mechanism of visible photon absorption: unveiling of the C 3 N 4–ZnO photoactive interface by means of EPR spectroscopy. Materials Advances 1 (7), 2357–2367.
Chen, H., Nanayakkara, C.E., Grassian, V.H., 2012. Titanium dioxide photocatalysis in atmospheric chemistry. Chem. Rev. 112 (11), 5919–5948.
Chen, W., Han, B., Tian, C., Liu, X., Liang, S., Deng, H., Lin, Z., 2019. MOFs-derived ultrathin holey Co3O4 nanosheets for enhanced visible light CO2 reduction. Appl. Catal. B Environ. 244, 996–1003.
Chen, X., Peng, X., Jiang, L., Yuan, X., Yu, H., Wang, H., Zhang, J., Xia, Q., 2020. Recent advances in titanium metal–organic frameworks and their derived materials: features, fabrication, and photocatalytic applications. Chem. Eng. J. 125080.
Deng, H., Fei, X., Yang, Y., Fan, J., Yu, J., Cheng, B., Zhang, L., 2021. S-scheme heterojunction based on p-type ZnMn2O4 and n-type ZnO with improved photocatalytic CO2 reduction activity. Chem. Eng. J. 409, 127377.
Dutta, V., Sharma, S., Raizada, P., Kumar, R., Thakur, V.K., Nguyen, V.-H., Asiri, A.M., Khan, A.A.P., Singh, P., 2020. Recent progress on bismuth-based Z-scheme semiconductor photocatalysts for energy and environmental applications. J. Environ. Chem. Eng. 8, 104505.
Ehsan, M.F., He, T., 2015. In situ synthesis of ZnO/ZnTe common cation heterostructure and its visible-light photocatalytic reduction of CO2 into CH4. Appl. Catal. B Environ. 166, 345–352.
Fox, M.A., 1983. Organic heterogeneous photocatalysis: chemical conversions sensitized by irradiated semiconductors. Acc. Chem. Res. 16 (9), 314–321.
Fresno, F., Villar-García, I.J., Collado, L., Alfonso-González, E., Reñones, P., Barawi, M., de la Peña O'Shea, V.c.A., 2018. Mechanistic view of the main current issues in photocatalytic CO2 reduction. J. Phys. Chem. Lett. 9 (24), 7192–7204.
Fu, J., Jiang, K., Qiu, X., Yu, J., Liu, M., 2020. Product selectivity of photocatalytic CO2 reduction reactions. Mater. Today 32, 222–243.
Fu, J., Xu, Q., Low, J., Jiang, C., Yu, J., 2019. Ultrathin 2D/2D WO3/g-C3N4 step-scheme H2-production photocatalyst. Appl. Catal. B Environ. 243, 556–565.
Fujishima, A., Inoue, T., Honda, K., 1979. Competitive photoelectrochemical oxidation of reducing agents at the titanium dioxide photoanode. J. Am. Chem. Soc. 101 (19), 5582–5588.
Ge, H., Xu, F., Cheng, B., Yu, J., Ho, W., 2019. S-scheme heterojunction TiO2/CdS nanocomposite nanofiber as H2-production photocatalyst. ChemCatChem 11 (24), 6301–6309.
Geng, Z., Kong, X., Chen, W., Su, H., Liu, Y., Cai, F., Wang, G., Zeng, J., 2018. Oxygen vacancies in ZnO nanosheets enhance CO2 electrochemical reduction to CO. Angew. Chem. 130 (21), 6162–6167.
Ghaemi-moghadam, M., Hasanzadeh, A., Rahmati, A., 2021. Charge transfer plasmon coupled surface photosensing in ZnO nanorods–Au array hetero-nanostructures. Opt Laser. Eng. 137, 106384.
Ghahramanifard, F., Rouhollahi, A., Fazlolahzadeh, O., 2018. Electrodeposition of Cu-doped p-type ZnO nanorods; effect of Cu doping on structural, optical and photoelectrocatalytic property of ZnO nanostructure. Superlattice. Microst. 114, 1–14.
Guo, Q., Fu, L., Yan, T., Tian, W., Ma, D., Li, J., Jiang, Y., Wang, X., 2020. Improved photocatalytic activity of porous ZnO nanosheets by thermal deposition graphene-like g-C3N4 for CO2 reduction with H2O vapor. Appl. Surf. Sci. 509, 144773.
Guo, Q., Zhang, Q., Wang, H., Liu, Z., Zhao, Z., 2016. Core-shell structured ZnO@ Cu-Zn–Al layered double hydroxides with enhanced photocatalytic efficiency for CO2 reduction. Catal. Commun. 77, 118–122.
Habisreutinger, S.N., Schmidt-Mende, L., Stolarczyk, J.K., 2013. Photocatalytic reduction of CO2 on TiO2 and other semiconductors. Angew. Chem. Int. Ed. 52 (29), 7372–7408.

Halmann, M., 1978. Photoelectrochemical reduction of aqueous carbon dioxide on p-type gallium phosphide in liquid junction solar cells. Nature 275 (5676), 115–116.
Hanahan, D., Coussens, L.M., 2012. Accessories to the crime: functions of cells recruited to the tumor microenvironment. Canc. Cell 21 (3), 309–322.
He, F., Meng, A., Cheng, B., Ho, W., Yu, J., 2020. Enhanced photocatalytic H2-production activity of WO3/TiO2 step-scheme heterojunction by graphene modification. Chin. J. Catal. 41 (1), 9–20.
Hegazy, I., Geioushy, R., El-Sheikh, S., Shawky, A., El-Sherbiny, S., Kandil, A.-H.T., 2020. Influence of oxygen vacancies on the performance of ZnO nanoparticles towards CO2 photoreduction in different aqueous solutions. Journal of Environmental Chemical Engineering 8 (4), 103887.
Huerta-Flores, A.M., Luévano-Hipólito, E., Torres-Martínez, L.M., Torres-Sánchez, A., 2019. Photocatalytic H 2 production and CO 2 reduction on Cu, Ni-doped ZnO: effect of metal doping and oxygen vacancies. J. Mater. Sci. Mater. Electron. 30 (20), 18506–18518.
Inoue, T., Fujishima, A., Konishi, S., Honda, K., 1979. Photoelectrocatalytic reduction of carbon dioxide in aqueous suspensions of semiconductor powders. Nature 277 (5698), 637–638.
Iqbal, M., Wang, Y., Hu, H., He, M., Shah, A.H., Li, P., Lin, L., Woldu, A.R., He, T., 2018a. Interfacial charge kinetics of ZnO/ZnTe heterostructured nanorod arrays for CO2 photoreduction. Electrochim. Acta 272, 203–211.
Iqbal, M., Wang, Y., Hu, H., He, M., Shah, A.H., Lin, L., Li, P., Shao, K., Woldu, A.R., He, T., 2018b. Cu2O-tipped ZnO nanorods with enhanced photoelectrochemical performance for CO2 photoreduction. Appl. Surf. Sci. 443, 209–216.
Iwantono, I., Nurwidya, W., Lestari, L., Naumar, F., Nafisah, S., Umar, A., Rahman, M., Salleh, M., 2015. Effect of growth temperature and time on the ZnO film properties and the performance of dye-sensitized solar cell (DSSC). J. Solid State Electrochem. 19 (4), 1217–1221.
Jamwal, D., Kaur, G., Raizada, P., Singh, P., Pathak, D., Thankur, P., 2020. Twin-Tail Surfactant Peculiarity in Superficial Fabrication of Semiconductor Quantum Dots: Toward Structural, Optical, and Electrical Features. J. Phys. Chem. C. 9, 5062–5073.
Jang, Y.J., Jang, J.-W., Lee, J., Kim, J.H., Kumagai, H., Lee, J., Minegishi, T., Kubota, J., Domen, K., Lee, J.S., 2015. Selective CO production by Au coupled ZnTe/ZnO in the photoelectrochemical CO2 reduction system. Energy Environ. Sci. 8 (12), 3597–3604.
Jin, C., Li, W., Chen, Y., Li, R., Huo, J., He, Q., Wang, Y., 2020. Efficient photocatalytic degradation and adsorption of tetracycline over type-II heterojunctions consisting of ZnO nanorods and K-doped exfoliated g-C3N4 nanosheets. Ind. Eng. Chem. Res. 59 (7), 2860–2873.
Karamian, E., Sharifnia, S., 2018. Enhanced visible light photocatalytic activity of BiFeO3-ZnO pn heterojunction for CO2 reduction. Mater. Sci. Eng. B 238, 142–148.
Karmee, S.K., Greiner, L., Kraynov, A., Müller, T.E., Niemeijer, B., Leitner, W., 2010. Nanoparticle catalysed oxidation of sulfides to sulfones by in situ generated H 2 O 2 in supercritical carbon dioxide/water biphasic medium. Chem. Commun. 46 (36), 6705–6707.
Kumar, A., Raizada, P., Hosseini-Bandegharaei, A., Thakur, V.K., Nguyen, V.-H., Singh, P., 2021. C-, N-Vacancy defect engineered polymeric carbon nitride towards photocatalysis: viewpoints and challenges. J. Mater. Chem. 9, 111–153.
Kumar, A., Raizada, P., Singh, P., Hosseini-Bandegharaei, A., Thakur, V.K., 2020a. Facile synthesis and extended visible light activity of oxygen and sulphur co-doped carbon nitride quantum dots modified Bi2MoO6 for phenol degradation. J. Photochem. Photobiol. Chem. 397, 112588.
Kumar, A., Raizada, P., Thakur, V.K., Saini, V., Khan, A.A.P., Singh, N., Singh, P., 2020b. An overview on polymeric carbon nitride assisted photocatalytic CO2 reduction: strategically manoeuvring solar to fuel conversion efficiency. Chem. Eng. Sci. 116219.
Kumar, R., Sudhaik, A., Raizada, P., Hosseini-Bandegharaei, A., Thakur, V.K., Saini, A., Saini, V., Singh, P., 2020c. An overview on bismuth molybdate based photocatalytic systems: controlled morphology and enhancement strategies for photocatalytic water purification. Journal of Environmental Chemical Engineering 8 (5), 104291.
Leitner, W., 1996. The coordination chemistry of carbon dioxide and its relevance for catalysis: a critical survey. Coord. Chem. Rev. 153, 257–284.
Li, M., Zhang, S., Li, L., Han, J., Zhu, X., Ge, Q., Wang, H., 2020. Construction of highly active and selective polydopamine modified hollow ZnO/Co3O4 pn heterojunction catalyst for photocatalytic CO2 reduction. Engineering ACS Sustainable Chemistry 8 (30), 11465–11476.
Li, P., Zhu, S., Hu, H., Guo, L., He, T., 2019. Influence of defects in porous ZnO nanoplates on CO2 photoreduction. Catal. Today 335, 300–305.
Li, X.-K., Ji, W.-J., Zhao, J., Wang, S.-J., Au, C.-T., 2005. Ammonia decomposition over Ru and Ni catalysts supported on fumed SiO2, MCM-41, and SBA-15. J. Catal. 236 (2), 181–189.
Li, X., Jiang, H., Ma, C., Zhu, Z., Song, X., Wang, H., Huo, P., Li, X., 2021. Local surface plasma resonance effect enhanced Z-scheme ZnO/Au/g-C3N4 film photocatalyst for reduction of CO2 to CO. Appl. Catal. B Environ. 283, 119638.
Li, X., Wang, Q., Zhao, Y., Wu, W., Chen, J., Meng, H., 2013. Green synthesis and photo-catalytic performances for ZnO-reduced graphene oxide nanocomposites. J. Colloid Interface Sci. 411, 69–75.
Lim, J., Monllor-Satoca, D., Jang, J.S., Lee, S., Choi, W., 2014. Visible light photocatalysis of fullerol-complexed TiO2 enhanced by Nb doping. Appl. Catal. B Environ. 152, 233–240.
Lin, L.-Y., Liu, C., Hsieh, T.-T., 2020. Efficient visible and NIR light-driven photocatalytic CO2 reduction over defect-engineered ZnO/carbon dot hybrid and mechanistic insights. J. Catal. 391, 298–311.
Lingampalli, S., Ayyub, M.M., Magesh, G., Rao, C., 2018. Photocatalytic reduction of CO2 by employing ZnO/Ag1-xCux/CdS and related heterostructures. Chem. Phys. Lett. 691, 28–32.
Liu, L., 2016. Controllable ZnO nanorod arrays@ carbon fibers composites: towards advanced CO2 photocatalytic reduction catalysts. Ceram. Int. 42 (10), 12516–12520.
Liu, S., Wang, J., Yu, J., 2016. ZIF-8 derived bimodal carbon modified ZnO photocatalysts with enhanced photocatalytic CO2 reduction performance. RSC Adv. 6 (65), 59998–60006.
Majumdar, P., Pant, D., Patra, S., 2017. Integrated photobioelectrochemical systems: a paradigm shift in artificial photosynthesis. Trends Biotechnol. 35 (4), 285–287.
Makino, H., Shimizu, H., 2018. Influence of crystallographic polarity on the opto-electrical properties of polycrystalline ZnO thin films deposited by magnetron sputtering. Appl. Surf. Sci. 439, 839–844.
Meng, J., Chen, Q., Lu, J., Liu, H., 2019. Z-scheme photocatalytic CO2 reduction on a heterostructure of oxygen-defective ZnO/reduced graphene oxide/UiO-66-NH2 under visible light. ACS Appl. Mater. Interfaces 11, 550–562.
Merino-Garcia, I., Albo, J., Solla-Gullon, J., Montiel, V., Irabien, A., 2019. Cu oxide/ZnO-based surfaces for a selective ethylene production from gas-phase CO2 electroconversion. Journal of CO2 Utilization 31, 135–142.
Modic, M., Kovač, J., Nicholls, J.R., Kos, Š., Serša, G., Cvelbar, U., Walsh, J.L., 2019. Targeted plasma functionalization of titanium inhibits polymicrobial biofilm recolonization and stimulates cell function. Appl. Surf. Sci. 487, 1176–1188.
Mohamad, A.A., Hassan, M.S., Yaakob, M.K., Taib, M.F.M., Badrudin, F.W., Hassan, O.H., Yahya, M.Z.A., 2017. First-principles calculation on electronic properties of zinc oxide by zinc–air system. Journal of King Saud University-Engineering Sciences 29 (3), 278–283.
Mori, K., Yamashita, H., Anpo, M., 2012. Photocatalytic reduction of CO2 with H2O on various titanium oxide photocatalysts. RSC Adv. 2, 3165–3172.
Morikawa, T., Asahi, R., Ohwaki, T., Aoki, K., Taga, Y., 2001. Band-gap narrowing of titanium dioxide by nitrogen doping. Jpn. J. Appl. Phys. 40 (6A), L561.
Mu, J., Teng, F., Miao, H., Wang, Y., Hu, X., 2020. In-situ oxidation fabrication of 0D/2D SnO2/SnS2 novel Step-scheme heterojunctions with enhanced photoelectrochemical activity for water splitting. Appl. Surf. Sci. 501, 143974.
Narváez, J.F., Grant, H., Gil, V.C., Porras, J., Sanchez, J.C.B., Duque, L.F.O., Sossa, R.R., Quintana-Castillo, J.C., 2019. Assessment of endocrine disruptor effects of levonorgestrel and its photoproducts: environmental implications of released fractions after their photocatalytic removal. J. Hazard Mater. 371, 273–279.
Nguyen, V.-H., Do, H.H., Van Nguyen, T., Singh, P., Raizada, P., Sharma, A., Sana, S.S., Grace, A.N., Shokouhimehr, M., Ahn, S.H., 2020. Perovskite oxide-based photocatalysts for solar-driven hydrogen production: progress and perspectives. Sol. Energy 211, 584–599.
Nie, N., He, F., Zhang, L., Cheng, B., 2018a. Direct Z-scheme PDA-modified ZnO hierarchical microspheres with enhanced photocatalytic CO2 reduction performance. Appl. Surf. Sci. 457, 1096–1102.
Nie, N., Zhang, L., Fu, J., Cheng, B., Yu, J., 2018b. Self-assembled hierarchical direct Z-scheme g-C3N4/ZnO microspheres with enhanced photocatalytic CO2 reduction performance. Appl. Surf. Sci. 441, 12–22. https://doi.org/10.1016/j.apsusc.2018.01.193.
Núñez, J., Víctor, A., Jana, P., Coronado, J.M., Serrano, D.P., 2013. Effect of copper on the performance of ZnO and ZnO1− xNx oxides as CO2 photoreduction catalysts. Catal. Today 209, 21–27.
Oliveira, J.A., Nogueira, A.E., Gonçalves, M.C., Paris, E.C., Ribeiro, C., Poirier, G.Y., Giraldi, T.R., 2018. Photoactivity of N-doped ZnO nanoparticles in oxidative and reductive reactions. Appl. Surf. Sci. 433, 879–886.
Osterloh, F.E., 2017. Photocatalysis versus photosynthesis: a sensitivity analysis of devices for solar energy conversion and chemical transformations. ACS Energy Letters 2 (2), 445–453.
Pare, B., Singh, P., Jonnalgadda, S.B., 2009. Degradation and mineralization of victoria blue B dye in a slurry photoreactor using advanced oxidation process. J. Sci. Ind. Res. 68, 724–729.
Patial, S., Hasija, V., Raizada, P., Singh, P., Singh, A.A.P.K., Asiri, A.M., 2020a. Tunable photocatalytic activity of SrTiO3 for water splitting: strategies and future scenario. Journal of Environmental Chemical Engineering 8 (3), 103791.
Patial, S., Raizada, P., Hasija, V., Singh, P., Thakur, V.K., Nguyen, V.-H., 2020b. Recent advances in photocatalytic multivariate metal organic framework (MOFs) based nanostructures toward renewable energy and the removal of environmental pollutants. Mater. Today Energy 19, 100589.
Rahmani, A.R., Salari, M., Shabanloo, A., Shabanloo, N., Bajalan, S., Vaziri, Y., 2020. Sono-catalytic activation of persulfate by nZVI-reduced graphene oxide for degradation of nonylphenol in aqueous solution: process optimization, synergistic effect and degradation pathway. Journal of Environmental Chemical Engineering 8 (5), 104202.
Raizada, P., Gautam, S., Priya, B., Singh, P., 2020. Preparation and photocatalytic activity of hydroxyapatite supported BiOCl nanocomposite for oxytetracyline removal. Adv. Mater. Lett. 7 (4), 312–318.
Raizada, P., Khan, A.A.P., Singh, P., 2020a. Construction of carbon nanotube mediated Fe doped graphitic carbon nitride and Ag3VO4 based Z-scheme heterojunction for H2O2 assisted 2, 4 dimethyl phenol photodegradation. Separ. Purif. Technol. 247, 116957.
Raizada, P., Kumar, A., Hasija, V., Singh, P., Thakur, V.K., Khan, A.A.P., 2020b. An overview of converting reductive photocatalyst into all solid-state and direct Z-scheme system for water splitting and CO2 reduction. J. Ind. Eng. Chem. 93, 1–27.
Raizada, P., Sharma, S., Kumar, A., Singh, P., Khan, A.A.P., Asiri, A.M., 2020c. Performance improvement strategies of CuWO4 photocatalyst for hydrogen generation and pollutant degradation. Journal of Environmental Chemical Engineering 104230.
Raizada, P., Sudhaik, A., Patial, S., Hasija, V., Khan, A.A.P., Singh, P., Gautam, S., Kaur, M., Nguyen, V.-H., 2020d. Engineering nanostructures of CuO-based

photocatalysts for water treatment: current progress and future challenges. Arabian Journal of Chemistry 13 (11), 8424–8457.
Raizada, P., Thakur, P., Sudhaik, A., Singh, P., Thakur, V.K., Hosseini-Bandegharaei, A., 2020e. Fabrication of dual Z-scheme photocatalyst via coupling of BiOBr/Ag/AgCl heterojunction with P and S co-doped g-C3N4 for efficient phenol degradation. Arabian Journal of Chemistry 13 (3), 4538–4552.
Rodríguez-González, V., Obregón, S., Patrón-Soberano, O.A., Terashima, C., Fujishima, A., 2020. An approach to the photocatalytic mechanism in the TiO2-nanomaterials microorganism interface for the control of infectious processes. Appl. Catal. B Environ. 270, 118853.
Sakakura, T., Choi, J.-C., Yasuda, H., 2007. Transformation of carbon dioxide. Chem. Rev. 107 (6), 2365–2387.
Samadi, M., Zirak, M., Naseri, A., Khorashadizade, E., Moshfegh, A.Z., 2016. Recent progress on doped ZnO nanostructures for visible-light photocatalysis. Thin Solid Films 605, 2–19.
Samarghandi, M.R., Tari, K., Shabanloo, A., Salari, M., Nasab, H.Z., 2020. Synergistic degradation of acid blue 113 dye in a thermally activated persulfate (TAP)/ZnO-GAC oxidation system: degradation pathway and application for real textile wastewater. Separ. Purif. Technol. 247, 116931.
Shao, X., Xin, W., Yin, X., 2017. Hydrothermal synthesis of ZnO quantum dot/KNb3O8 nanosheet photocatalysts for reducing carbon dioxide to methanol. Beilstein J. Nanotechnol. 8 (1), 2264–2270.
Sharma, S., Dutta, V., Raizada, P., Hosseini-Bandegharaei, A., Singh, P., Nguyen, V.-H., 2020. Tailoring cadmium sulfide-based photocatalytic nanomaterials for water decontamination: a review. Environ. Chem. Lett. 1–36.
Shen, J., Chen, Z., Han, S., Zhang, H., Xu, H., Xu, C., Ding, Z., Yuan, R., Chen, J., Long, J., 2020b. Plasmonic Electrons-Driven Solar-to-Hydrocarbon Conversion over Au NR@ ZnO Core-Shell Nanostructures. ChemCatChem.
Shen, D., Li, X., Ma, C., Zhou, Y., Sun, L., Yin, S., Huo, P., Wang, H., 2020a. Synthesized Z-scheme photocatalyst ZnO/gC 3 N 4 for enhanced photocatalytic reduction of CO 2. New J. Chem. 44 (38), 16390–16399.
Shi, R., Waterhouse, G.I., Zhang, T., 2017. Recent progress in photocatalytic CO2 reduction over perovskite oxides. Solar RRL 1 (11), 1700126.
Shkrob, I.A., Marin, T.W., He, H., Zapol, P., 2012. Photoredox reactions and the catalytic cycle for carbon dioxide fixation and methanogenesis on metal oxides. J. Phys. Chem. C 116 (17), 9450–9460.
Shokoohi, R., Salari, M., Shabanloo, A., Shabanloo, N., Marofi, S., Faraji, H., Vanaei Tabar, M., Moradnia, M., 2020. Catalytic activation of persulphate with Mn3O4 nanoparticles for degradation of acid blue 113: process optimisation and degradation pathway. Int. J. Environ. Anal. Chem. 1–20.
Singh, G., Lee, J., Karakoti, A., Bahadur, R., Yi, J., Zhao, D., AlBahily, K., Vinu, A., 2020. Emerging trends in porous materials for CO 2 capture and conversion. Chem. Soc. Rev. 49 (13), 4360–4404.
Singh, V., Beltran, I.J.C., Ribot, J.C., Nagpal, P., 2014. Photocatalysis deconstructed: design of a new selective catalyst for artificial photosynthesis. Nano Lett. 14 (2), 597–603.
Singh, P., Raizada, P., Pathania, D., Kumar, Amit, Thankur, Pankaj, 2013. Preparation of BSA-ZnWO$_4$ Nanocomposites with Enhanced Adsorptional Photocatalytic Activity for Methylene Blue Degradation. Int. J. Photoenergy. 2013, 726250.
Singh, P., Raizada, P., Pathania, D., Sharma, G., Sharma, P., 2013. Microwave induced KOH activation of guava peel carbon as an adsorbent for congo red dye removal from aqueous phase. Indian J. Chem. Technol. 20, 305–311.
Solangi, K., Islam, M., Saidur, R., Rahim, N., Fayaz, H., 2011. A review on global solar energy policy. Renew. Sustain. Energy Rev. 15 (4), 2149–2163.
Stelo, F., Kublik, N., Ullah, S., Wender, H., 2020. Recent advances in Bi2MoO6 based Z-scheme heterojunctions for photocatalytic degradation of pollutants. J. Alloys Compd. 829, 154591.
Subrahmanyam, M., Kaneco, S., Alonso-Vante, N., 1999. A screening for the photo reduction of carbon dioxide supported on metal oxide catalysts for C1–C3 selectivity. Appl. Catal. B Environ. 23 (2–3), 169–174.
Sudhaik, A., Raizada, P., Thakur, S., Saini, R.V., Saini, A.K., Singh, P., Thakur, V.K., Nguyen, V.-H., Khan, A.A.P., Asiri, A.M., 2020. Synergistic photocatalytic mitigation of imidacloprid pesticide and antibacterial activity using carbon nanotube decorated phosphorus doped graphitic carbon nitride photocatalyst. Journal of the Taiwan Institute of Chemical Engineers 113, 142–154.
Sun, Z., Fan, Q., Zhang, M., Liu, S., Tao, H., Texter, J., 2019. Supercritical fluid-facilitated exfoliation and processing of 2D materials. Advanced Science 6 (18), 1901084.
Sun, Z., Talreja, N., Tao, H., Texter, J., Muhler, M., Strunk, J., Chen, J., 2018. Catalysis of carbon dioxide photoreduction on nanosheets: fundamentals and challenges. Angew. Chem. Int. Ed. 57 (26), 7610–7627.
Taraka, T.P.Y., Gautam, A., Jain, S.L., Bojja, S., Pal, U., 2019. Controlled addition of Cu/Zn in hierarchical CuO/ZnO pn heterojunction photocatalyst for high photoreduction of CO2 to MeOH. Journal of CO2 Utilization 31, 207–214.
Thakur, P., Raizada, P., Singh, P., Kumar, A., Khan, A.A.P., Asiri, A.M., 2020. Exploring recent advances in silver halides and graphitic carbon nitride-based photocatalyst for energy and environmental applications. Arabian Journal of Chemistry 13 (11), 8271–8300.
Tiegel, M., Hosseinabadi, R., Kuhn, S., Herrmann, A., Rüssel, C., 2015. Young′ s modulus, Vickers hardness and indentation fracture toughness of alumino silicate glasses. Ceram. Int. 41 (6), 7267–7275.
Vickers, N.J., 2017. Animal communication: when i'm calling you, will you answer too? Curr. Biol. 27 (14), R713–R715.
Vogel, D., Krüger, P., Pollmann, J., 1995. Ab initio electronic-structure calculations for II-VI semiconductors using self-interaction-corrected pseudopotentials. Phys. Rev. B 52 (20), R14316.
Wang, C., Ranasingha, O., Natesakhawat, S., Ohodnicki, P.R., Andio, M., Lewis, J.P., Matranga, C., 2013. Visible light plasmonic heating of Au–ZnO for the catalytic reduction of CO2. Nanoscale 5 (15), 6968–6974.
Wang, H.-T., Liu, Y.-P., Zhang, H., Chang, N., Shao, W., Shi, M.-S., Ao, D., Lu, M.-C., 2019. Design and synthesis of porous C–ZnO/TiO2@ ZIF-8 multi-component nano-system via pyrolysis strategy with high adsorption capacity and visible light photocatalytic activity. Microporous Mesoporous Mater. 288, 109548.
Wang, T., Shi, L., Tang, J., Malgras, V., Asahina, S., Liu, G., Zhang, H., Meng, X., Chang, K., He, J., 2016. A Co 3 O 4-embedded porous ZnO rhombic dodecahedron prepared using zeolitic imidazolate frameworks as precursors for CO 2 photoreduction. Nanoscale 8 (12), 6712–6720.
Wang, X., Li, Q., Zhou, C., Cao, Z., Zhang, R., 2019. ZnO rod/reduced graphene oxide sensitized by α-Fe2O3 nanoparticles for effective visible-light photoreduction of CO2. J. Colloid Interface Sci. 554, 335–343.
Wang, Z.-j., Song, H., Pang, H., Ning, Y., Dao, T.D., Wang, Z., Chen, H., Weng, Y., Fu, Q., Nagao, T., 2019. Photo-assisted methanol synthesis via CO2 reduction under ambient pressure over plasmonic Cu/ZnO catalysts. Appl. Catal. B Environ. 250, 10–16.
Won, D.-I., Lee, J.-S., Ji, J.-M., Jung, W.-J., Son, H.-J., Pac, C., Kang, S.O., 2015. Highly robust hybrid photocatalyst for carbon dioxide reduction: tuning and optimization of catalytic activities of dye/TiO2/Re (I) organic–inorganic ternary systems. J. Am. Chem. Soc. 137 (42), 13679–13690.
Wu, K., Dong, X., Zhu, J., Wu, P., Liu, C., Wang, Y., Wu, J., Hou, J., Liu, Z., Guo, X., 2018a. Designing biomimetic porous celery: TiO 2/ZnO nanocomposite for enhanced CO 2 photoreduction. J. Mater. Sci. Mater. Electron. 53 (16), 11595–11606.
Wu, Z.-Y., Ji, W.-B., Hu, B.-C., Liang, H.-W., Xu, X.-X., Yu, Z.-L., Li, B.-Y., Yu, S.-H., 2018b. Partially oxidized Ni nanoparticles supported on Ni-N co-doped carbon nanofibers as bifunctional electrocatalysts for overall water splitting. Nanomater. Energy 51, 286–293.
Xi, G., Ouyang, S., Li, P., Ye, J., Ma, Q., Su, N., Bai, H., Wang, C., 2012. Ultrathin W18O49 nanowires with diameters below 1 nm: synthesis, near-infrared absorption, photoluminescence, and photochemical reduction of carbon dioxide. Angew. Chem. Int. Ed. 51 (10), 2395–2399.
Xia, S., Meng, Y., Zhou, X., Xue, J., Pan, G., Ni, Z., 2016. Ti/ZnO–Fe2O3 composite: synthesis, characterization and application as a highly efficient photoelectrocatalyst for methanol from CO2 reduction. Appl. Catal. B Environ. 187, 122–133.
Xiao, J., Frauenheim, T., 2013. Theoretical insights into CO2 activation and reduction on the Ag (111) monolayer supported on a ZnO (000 1) substrate. he Journal of Physical Chemistry C 117 (4), 1804–1808.
Xu, Q., Yu, J., Zhang, J., Zhang, J., Liu, G., 2015. Cubic anatase TiO 2 nanocrystals with enhanced photocatalytic CO 2 reduction activity. Chem. Commun. 51 (37), 7950–7953.
Xue, W., Huang, D., Wen, X., Chen, S., Cheng, M., Deng, R., Li, B., Yang, Y., Liu, X., 2020. Silver-based semiconductor Z-scheme photocatalytic systems for environmental purification. J. Hazard Mater. 390, 122128.
Yahaya, A., Gondal, M., Hameed, A., 2004. Selective laser enhanced photocatalytic conversion of CO2 into methanol. Chem. Phys. Lett. 400 (1–3), 206–212.
Yang, C., Li, Q., Xia, Y., Lv, K., Li, M., 2019a. Enhanced visible-light photocatalytic CO2 reduction performance of Znln2S4 microspheres by using CeO2 as cocatalyst. Appl. Surf. Sci. 464, 388–395.
Yang, C., Liu, D., Chen, Y., Chen, C., Wang, J., Fan, Y., Huang, S., Lei, W., 2019b. Three-dimensional functionalized boron nitride nanosheets/ZnO superstructures for CO2 capture. ACS Appl. Mater. Interfaces 11 (10), 10276–10282.
Yu, W., Xu, D., Peng, T., 2015. Enhanced photocatalytic activity of gC3N4 for selective CO2 reduction to CH3OH via facile coupling of ZnO: a direct Z-scheme mechanism. J. Mater. Chem. 3 (39), 19936–19947.
Zhang, F., Li, Y.-H., Qi, M.-Y., Tang, Z.-R., Xu, Y.-J., 2020. Boosting the activity and stability of Ag-Cu2O/ZnO nanorods for photocatalytic CO2 reduction. Appl. Catal. B Environ. 268, 118380.
Zhang, W., Mohamed, A.R., Ong, W.J., 2020. Z-Scheme photocatalytic systems for carbon dioxide reduction: where are we now? Angew. Chem. Int. Ed. 59 (51), 22894–22915.
Zhao, J., Liu, B., Meng, L., He, S., Yuan, R., Hou, Y., Ding, Z., Lin, H., Zhang, Z., Wang, X., 2019. Plasmonic control of solar-driven CO2 conversion at the metal/ZnO interfaces. Appl. Catal. B Environ. 256, 117823.
Zheng, X., Zhang, Z., Meng, S., Wang, Y., Li, D., 2020. Regulating charge transfer over 3D Au/ZnO hybrid inverse opal toward efficiently photocatalytic degradation of bisphenol A and photoelectrochemical water splitting. Chem. Eng. J. 393, 124676.
Zhu, S., Wang, D., 2017. Photocatalysis: basic principles, diverse forms of implementations and emerging scientific opportunities. Advanced Energy Materials 7 (23), 1700841.
Zubair, M., Razzaq, A., Grimes, C.A., S, I., 2017. Cu2ZnSnS4 (CZTS)-ZnO: a noble metal-free hybrid Z-scheme photocatalyst for enhanced solar-spectrum photocatalytic conversion of CO2 to CH4. Journal of CO2 Utilization 20, 301–311.